Selective TASK-1 Inhibitor with a Defined Structure−Activity Relationship Reduces Cancer Cell Proliferation and Viability

Bárbara Arévalo,[∞] Mauricio Bedoya,[∞] Aytug K. Kiper,[∞] Fernando Vergara, David Ramírez, Yuliet Mazola, Daniel Bustos, Rafael Zúñiga, Rocio Cikutovic, Angel Cayo, Susanne Rinné, M. Teresa Ramirez-Apan, Francisco V. Sepúlveda, Oscar Cerda, Eduardo López-Collazo, Niels Decher,[*] Leandro Zúñiga,[*] Margarita Gutierrez,[*] and Wendy González[*]

ACCESS | Metrics & More | Article Recommendations | Supporting Information

ABSTRACT: Chemical structures of selective blockers of TASK channels contain aromatic groups and amide bonds. Using this rationale, we designed and synthesized a series of compounds based on 3-benzamidobenzoic acid. These compounds block TASK-1 channels by binding to the central cavity. The most active compound is 3-benzoylamino-N-(2-ethyl-phenyl)-benzamide or **F3**, blocking TASK-1 with an IC_{50} of 148 nM, showing a reduced inhibition of TASK-3 channels and not a significant effect on different K^+ channels. We identified putative F3-binding sites in the TASK-1 channel by molecular modeling studies. Mutation of seven residues to A (I118A, L122A, F125A, Q126A, L232A, I235A, and L239A) markedly decreased the F3-induced inhibition of TASK-1 channels, consistent with the molecular modeling predictions. **F3** blocks cell proliferation and viability in the MCF-7 cancer cell line but not in TASK-1 knockdown MCF-7 cells, indicating that it is acting in TASK-1 channels. These results indicated that TASK-1 is necessary to drive proliferation in the MCF-7 cancer cell line.
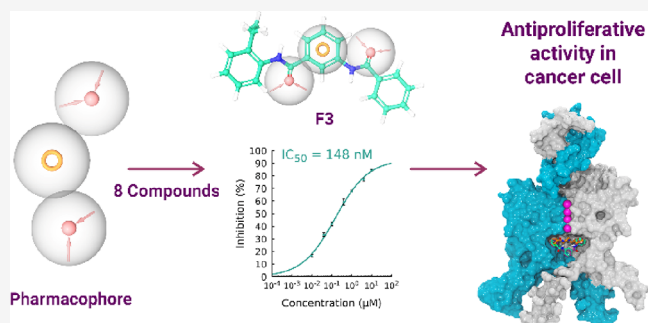
INTRODUCTION

Two-pore domain potassium channels (K_{2P} channels) are typically constitutively active channels that enable leak potassium (K^+) currents in different cell types from a variety of tissues.[1] K_{2P} currents play important roles in multiple cellular functions such as the maintenance of resting membrane potential, the counterbalance of action potential depolarization, the regulation of cell volume, differentiation, proliferation, migration, and apoptosis.[2] In mammals, the K_{2P} family has 15 members grouped into six subfamilies (TWIK, TREK, TASK, TALK, THIK, and TRESK). Structurally, K_{2P} channels have unique membrane topologies consisting of two pore-forming regions (P1−P2) flanked by four transmembrane domains (S1−S4).[3] They assemble into dimers, which can be homo- or heterodimers, increasing the diversity of K^+ channel functional properties.[4]

Since K_{2P} channels are involved in a wide number of cellular processes, they have been related to several pathologies in humans, including cancer. Their expression has been found to be abnormal in many types of tumors and cancer cells.[5,6] Most research connecting K_{2P} channels and cancer has been done on TASK-3, also known as $K_{2P}9.1$, a member of the TASK (TWIK-related acid-sensitive K^+ channel) subfamily. TASK-3 conducts outwardly rectifying currents, which are modulated by chemical and physical stimuli such as acidification and hypoxia.[7,8]

Interestingly, it is well documented that *KCNK9* (encoding TASK-3) is an established proto-oncogene[9] whose amplification has been reported in a number of cancers such as breast,[10] prostate, and lung cancers as well as malignant melanomas,[11] ovarian carcinoma,[12] gastric carcinoma,[13] and colorectal carcinomas.[14] It has been proposed that TASK-3 overexpression favors the survival of tumor cells by increasing their resistance to hypoxia and serum deprivation in the poorly oxygenated areas of solid tumors, which may explain its tumorigenic properties.[9] In fact, TASK-3 is a tumor marker and therapeutic target in ovarium cancer; TASK-3 blockers cause significant reduction in cell proliferation and increase apoptosis in SKOV-3 and OVCAR-3 ovarian cancer cell lines.[12]
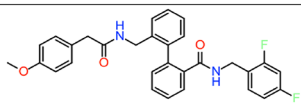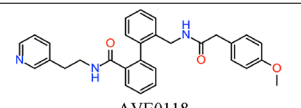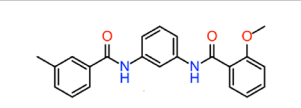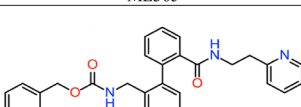
Besides TASK-3, TASK-1 was recently found to promote pivotal events in cancer cell invasion and metastasis.[15] In humans, TASK-1 (also known as $K_{2P}3.1$) shares 58.9% amino acid sequence identity with TASK-3 and is also highly sensitive

to extracellular pH.[8,16] TASK-1 mediates outward rectified potassium current and its codifying gene *KCNK3* shows a differential expression in breast, kidney, leukemia, lymphoma, colorectal, and lung cancers compared to normal tissues,[6] suggesting a role for TASK-1 in the pathogenesis of some human carcinomas. In the case of lung cancer, Leithner *et al.* showed that inhibition of TASK-1 enhances apoptosis and reduces proliferation in non-small-cell lung cancer (NSCLC) cells.[17] Also, TASK-1 overexpression promotes epithelial–mesenchymal transition (EMT) in the NSCLC cell line A549.[15] EMT is a process that converts epithelial cells into mesenchymal cells through disruption of cell–cell junctions and extensive reorganization of the actin cytoskeleton. This process is required for tumor invasion and metastasis and also contributes to the resistance of tumoral cells to therapeutic agents.[15] The discovery of a role of TASK-1 in EMT of NSCLC cells makes it attractive as a target, considering that EMT is common to other cancer types such as breast cancer.[18]

The above-mentioned evidence of a linkage between the TASK-1 channel activity and cancer implies that TASK-1 blockers could be of therapeutic relevance in this disease. Since the TASK members, TASK-1 and TASK-3, are expressed in many tissues, their pharmacological manipulation must be undertaken with care. In addition, to be most effective, TASK channels demand individual blockers to be used, for instance, in personalized medicine. However, most available TASK blockers do not distinguish between TASK-1 and TASK-3. Some success in the design of selective TASK-1 inhibitors has been achieved.[19] Such compounds comprise a bisamide core and an aromatic ring and include A1899,[20] AVE0118, S9947,[21] and ML365.[22] A1899 and ML365 have shown selectivity for TASK-1 (Table 1).

Table 1. Bisamide Blockers of the TASK-1 Channel

Compound	TASK-1 IC$_{50}$ (μM)	Cell line	Ref
A1899	0.035 ± 0.003	*X.* oocytes	20
AVE0118	0.6	*X.* oocytes	21
ML365	0.016	CHO cells	22
S9947	0.2	*X.* oocytes	21

The need for highly discriminating TASK-1 inhibitors for a better characterization of the physiological role of this channel and also for its usage as a drug target is critical. Currently, only a few compounds block TASK-1 channels in the submicromolar range: A1899 (IC$_{50}$ = 0.035 μM), A293 (IC$_{50}$ = 0.2 μM),[21] S9947 (IC$_{50}$ = 0.2 μM), Bayer compounds (EC$_{50}$ = 9.5 and 7.6 nM),[23] and ML365 (IC$_{50}$ = 0.016 μM).

In the present work, we have designed a novel series of eight bisamide-derived compounds (named **F1**−**F8**) starting from 3-benzamidobenzoic acid. We expressed TASK-1 and TASK-3 in *Xenopus laevis* oocytes and evaluated **F1-F8** inhibitory activity using two-electrode voltage clamp (TEVC). The compound 3-benzoylamino-*N*-(2-ethyl-phenyl)-benzamide or **F3** blocks TASK-1 with an IC$_{50}$ of 148 nM, while it shows only a minor inhibition of TASK-3. In addition, we studied other representative K$^+$ channels and found that **F3** does not produce a significant effect on their currents. Since TASK-1 is overexpressed in breast cancer *versus* normal tissue,[6] and there is still a need for new therapeutic options to reduce mortality associated with this disease, we investigated the effect of our novel selective TASK-1 inhibitor **F3** on cell proliferation and viability in the MCF-7 breast cancer cell line. Both TASK-1 and TASK-3 are expressed in MCF-7 cells, although TASK-3 exhibits higher mRNA levels.[24] We knocked down the expression of TASK-1 and TASK-3 in MCF-7 cells with short hairpin RNA (shRNA)[25] to evaluate the effect of **F3**. Cell counting and viability assays indicated that knockdown of TASK-3 decreased the ability of cell proliferation and cell viability after 48 and 72 h of incubation with **F3**. However, knocked-down cells of TASK-1 do not show decreased cell proliferation and viability values in contrast with wild-type MCF-7 cells. Our results suggest that targeting TASK-1 might also be promising for breast cancer treatment.

■ RESULTS

Compound Rational Design. Ramírez *et al.*[26] built four homology models of the TASK-1 channel. We used these models and built also four new models of the TASK-3 channel. On the other hand, we design 30 derivatives based on a head compound (Figure 1a). All of them were subjected to molecular docking in TASK-1 and TASK-3 structures, and the poses were organized using clustering. We selected eight compounds to be synthesized, which corresponds to the compounds present in more conformational clusters in TASK-1 and TASK-3 channels (Table S1).

Synthesis of Compounds. The synthesis of the head compound was carried out following the described methodology (Hosangadi and Dave[27]), obtaining compound (**E**), and the reaction is summarized in Scheme 1.

Compound **E** was used as a basis for the formation of a new amide group using the available acid function through a second amidation.[27] The use of different amines allowed the generation of structural diversity in the obtained compounds (**F1**−**F8**) (Scheme 2 and Figure 1a).

The products obtained were purified by column chromatography and characterized by spectroscopic methods (NMR). The signals obtained using NMR agreed with the proposed structures. Products **F1**−**F8** were obtained in 55−85% yield.

Biological Evaluation. All compounds were subjected to two-electrode voltage-clamp measurements to evaluate them as potential TASK channel inhibitors following the methodology described by Streit *et al.*[20] The eight bisamide compounds synthesized were evaluated at 10 μM and were seen to decrease TASK currents on different extents (Figure 2).

Compound **F3** was the most potent, and compound **F4** was the least potent. These two compounds correspond to those with the most extreme activities (Figure 2b). To further study the activity of the compounds, the four compounds with the highest activity at 10 μM (**F2**, **F3**, **F5**, and **F6**) were selected to perform a dose−activity curve and to obtain the IC$_{50}$ value. In
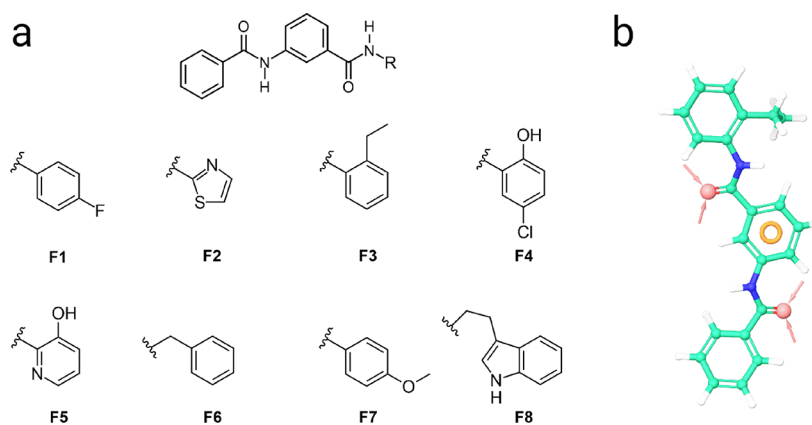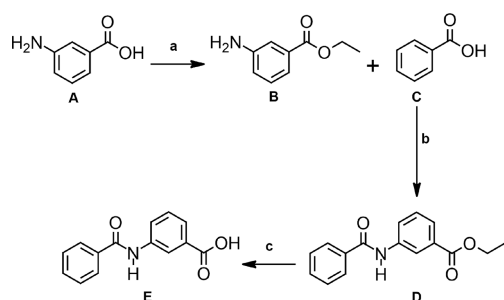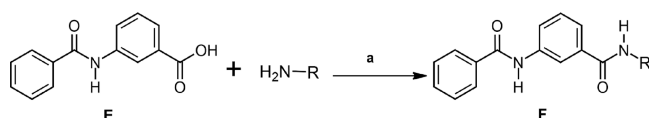
Figure 1. Series of synthesized compounds (a) and common pharmacophore (b). The common pharmacophore is shown in the structure of compound **F3**. The hydrogen-bond acceptor groups are shown in pink spheres and the aromatic ring in an orange torus.

Scheme 1. Synthesis of the Head Compound (E)[a]

[a](a) $SOCl_2$, EtOH, room temperature (10−18 h). (b) CH_2Cl_2, $SOCl_2$, 60 °C, reflux (1−2 h). (c) $MeOH:H_2O$ (2:1), LiOH, room temperature, stirring (2−4 h), 83−91% overall yield.

Scheme 2. Synthesis of the Eight Compounds[a]

[a](a) CH_2Cl_2, $SOCl_2$, 60 °C, reflux (12 h). The synthesis was carried out following the methodology described by Hosangadi and Dave,[27] obtaining the derivatives (**F**).

the case of TASK-1 compounds, **F2** and **F3** were the most active of the series, and the dose−activity curve showed IC_{50} values of 388 and 148 nM, respectively (Figure 3a). Compounds **F3** and **F2** showed also higher activity on TASK-3 with IC_{50} values of 1.75 and ∼7.17 μM, respectively.
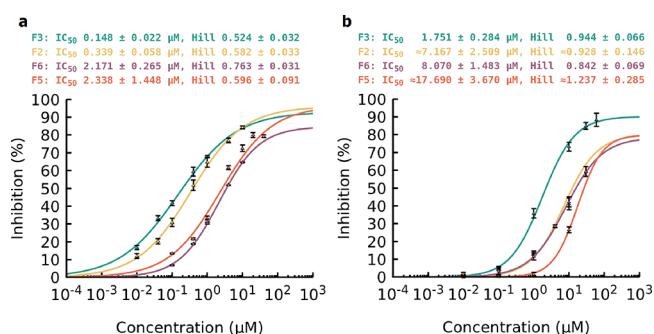

Figure 3. Concentration−response curve (CRC) of compounds **F2**, **F3**, **F5**, and **F6** over (a) TASK-1 and (b) TASK-3 channels. Blockade was analyzed after the execution of the protocol at the end of the +40 mV pulse at concentrations of 0.01 to 10 μM. $n = 4−8$. All data are presented as the mean ± SEM. Dashed lines indicate an approximated CRC.
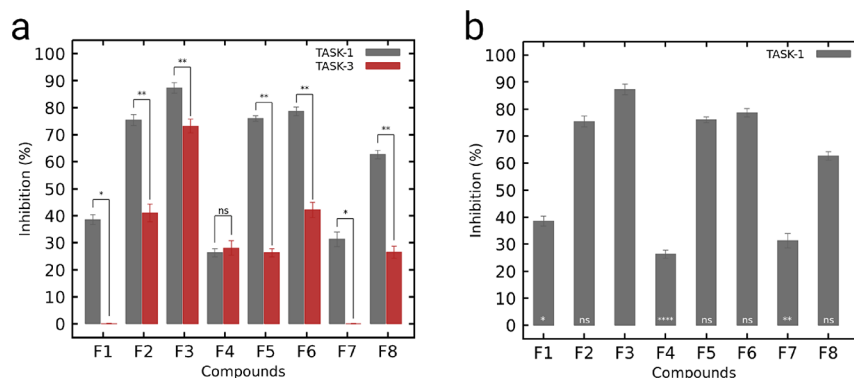
Figure 2. Inhibitory activity of synthesized compounds evaluated on TASK-1 and TASK-3 channels. Data obtained by the TEVC technique at a concentration of 10 μM. $n = 5$ except for compounds **F1** and **F7** in TASK-3 ($n = 3$). Data are presented as the mean ± SEM. (a) The significance levels (comparing TASK-1 and TASK-3 in each group) are shown as follows: ****$p < 0.0001$, ***$p < 0.001$, **$p < 0.01$, *$p < 0.05$, ns = no significant difference, using a pairwise comparison with the Kruskal−Wallis test. (b) A comparison was made between **F3** and all compounds in TASK-1 using the Kruskal−Wallis and Nemenyi post-test for multiple comparisons. The level of significance is the same as the previous one.
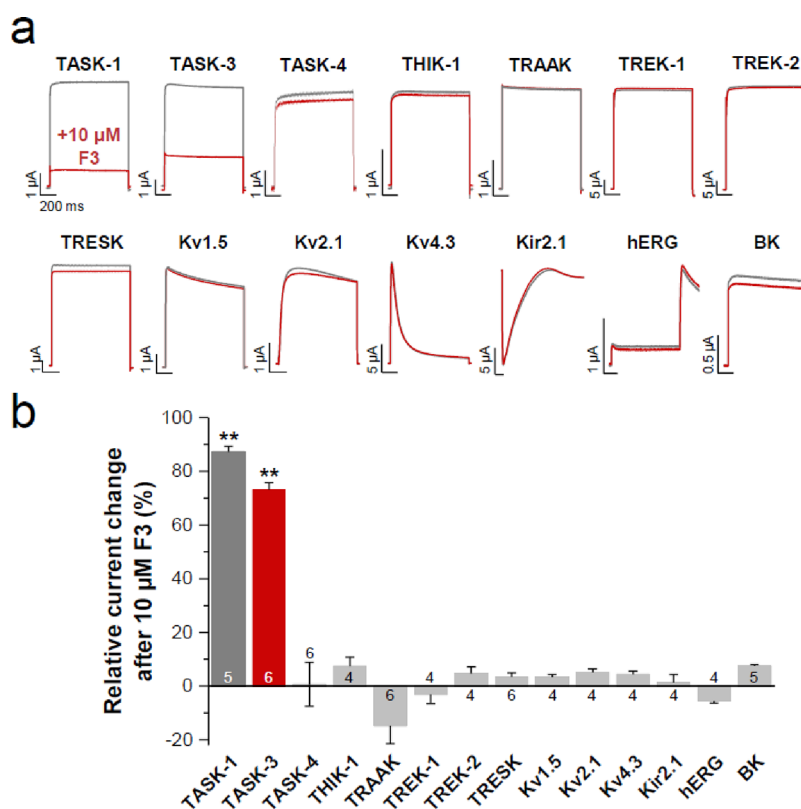
Figure 4. Activity of compound **F3** on different K⁺ channels. (a) Representative voltage-clamp recordings of *Xenopus* oocytes expressing a variety of K⁺ channels before and after 10 μM **F3** application. (b) Analysis of relative current changes after 10 μM **F3** application. All data are presented as the mean $\pm$ SEM. The number of biological replicates (n) is illustrated in the respective bar graphs. Paired Student's *t*-test was applied to raw currents before and after drug application for each channel individually. **$p < 0.01$.
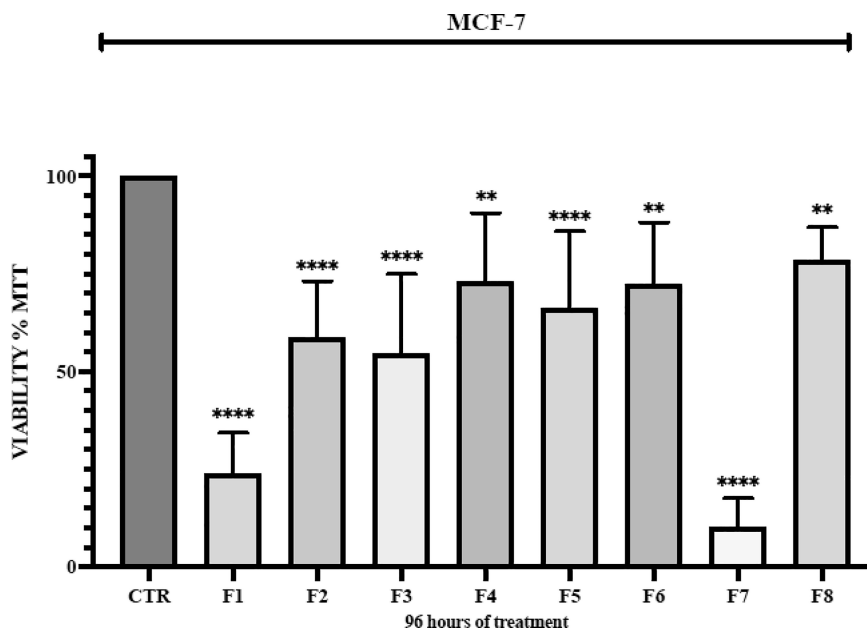
Figure 5. Antiproliferative activity in the MCF-7 cell line. Compounds were evaluated at a concentration of 10 μM. $n = 8$. Data are presented as the mean $\pm$ SEM. The significance levels are shown as follows: ****$p < 0.0001$, ***$p < 0.001$, **$p < 0.01$, *$p < 0.05$ based on ANOVA with Dunnett's post-test.

To verify the selectivity, the effect of compound **F3** was tested on other potassium channels. In contrast to the results with TASK-1 and TASK-3, **F3** (10 μM) showed a nonsignificant change in currents encoded by other K⁺ channels (Figure 4).

Viability Assays. To explore the effectiveness of our compounds concerning the decrease in cell proliferation, we performed cytotoxicity measurements of all compounds in tumor cell lines. The anti-oncogenic effect of the compounds was explored in a cell line of mammary origin (MCF-7) using the

Figure 6. Effect of compound **F3** on cell proliferation and viability in TASK-1 knockdown. (a) Proliferation of MCF-7 cells and cells transduced with shRNAs against TASK-1 (knockdown A, 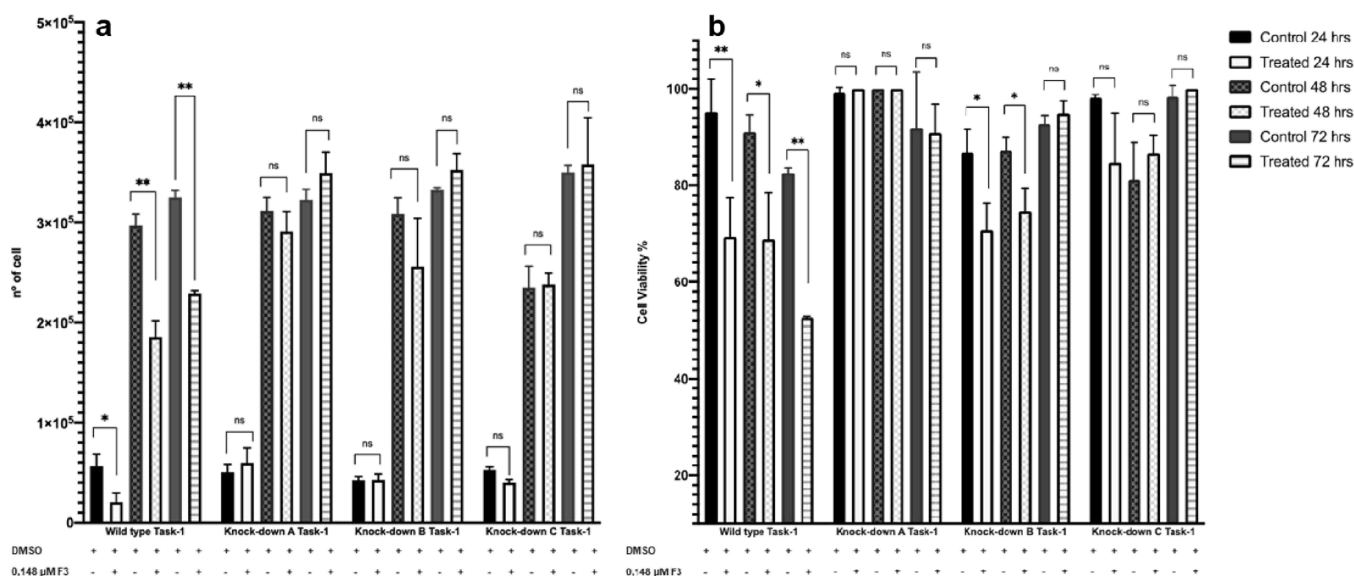B, and C) after 24, 48, and 72 h of incubation with DMSO treatment $(+/-)$ or DMSO and **F3** treatment $(+/+)$. (b) Percentage of the cell viability of MCF-7 cells under the indicated conditions following 24, 48, and 72 h of incubation. Error bars represent the mean $\pm$ SEM of three independent experiments. ****$p < 0.0001$, ***$p < 0.001$, **$p < 0.01$, *$p < 0.05$, ns = no significant difference compared with the control based on two-way ANOVA with Tukey's post-test.
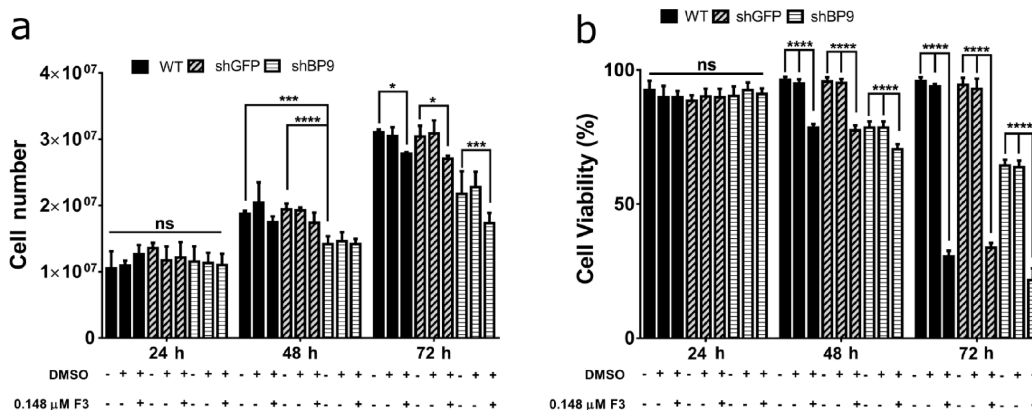

Figure 7. Effect of compound **F3** on cell proliferation and viability in TASK-3 knockdown. (a) Proliferation of wild-type (WT) MCF-7 cells or the same cells transduced with shRNAs against GFP (shGFP) or TASK-3 (shBP9) after 24, 48, and 72 h of incubation with no treatment $(-/-)$, DMSO treatment $(+/-)$, or F3 treatment $(+/+)$. (b) Percentage of the viability of MCF-7 cells under the indicated conditions following 24, 48, and 72 h of incubation. Error bars represent the mean $\pm$ SEM of three independent experiments. ****$p < 0.0001$, ***$p < 0.001$, **$p < 0.01$, *$p < 0.05$, ns = no significant difference compared with WT based on two-way ANOVA with Tukey's post-test.

MTT staining method.[28] The screening of the synthesized compounds was done at 10 μM, which is the concentration used in electrophysiological assays to test all compounds (Figure 2).

Compound **F3** showed an antiproliferative activity of $\sim$45% on the cell line MCF-7 (Figure 5). **F1** and **F7** were not considered since despite having the highest antiproliferative activity, they only showed inhibition values of 25 and 10% at 10 μM on TASK-1 channels in electrophysiological recordings, respectively. Probably their cytotoxic activity is mediated by a metabolic pathway that involves different therapeutic targets from our objective of study.

TASK-1 Silencing by Short Hairpin RNA (shRNA). The possible role of TASK-1 in the effect of compound **F3** in MCF-7 cells was investigated by assays of cell proliferation and viability after shRNA knockdown of the channel. Four groups of cells were used: untreated MCF-7 cells and MCF-7 cells treated with three different shRNA constructs against TASK-1. A decrease in

the levels of TASK-1 was observed by real-time PCR and immunofluorescence in the three different shRNA constructs against TASK-1 (knockdown A → shAP3, knockdown B → shBP3, and knockdown C → shCP3, Figures S1 and S2). Cells transduced with constructs A and C show a significant mRNA level decrease compared to wild-type MCF-7 cells, and there are no significant differences in the proliferation and viability of MCF-7 cells with the TASK-1 knockdown (Figure S3).

Experiments run in parallel cells were assayed after 24, 48, and 72 h of incubation with **F3** at 0.148 μM (IC$_{50}$ for TASK-1 inhibition with **F3** in *X. laevis* oocytes, Figure 3). Figure 6 shows the results of TASK-1 knockdown on the proliferation and viability of MCF-7 cells. MCF-7 cells show a significant decrease in their proliferation and viability in the presence of **F3** compared to MCF-7 cells that were treated only with the vehicle (DMSO). On the other hand, the cells with knockdown for TASK-1 do not show significant differences in proliferation and

viability when treated with **F3** or the vehicle at different hours after treatment, except for the viability of construct B at 24 and 48 h, which is consistent with a nonsignificant decrease in mRNA levels with respect to wild-type MCF-7 cells (Figure S1). These results demonstrate that **F3** treatment has a potent effect on the cell proliferation and viability of MCF-7 cells, probably by TASK-1 channel blocking.

TASK-3 Silencing by Short Hairpin RNA (shRNA). As TASK-3 is also blocked by **F3** but in a lower quantity as TASK-1 (Figure 2a), with a 12-fold higher IC_{50} for TASK-3 (Figure 3), we aimed to discard the possibility that **F3** is acting in MCF-7 cells also by blocking TASK-3. Three groups of cells were used: untransfected MCF-7 cells, cells previously treated with a control shRNA directed against GFP (shGFP) and therefore deemed to be a further control, and cells previously transduced with shBP9 to knock down TASK-3 expression (shBP9). Experiments of cell proliferation and viability were run as for TASK-1 knockdown experiments. Figure 7 shows the results of TASK-3 knockdown on the proliferation and viability of MCF-7 cells. No significant differences are observed in the cell proliferation and viability between the WT, shGFP, and shBP9 cells after 24 h of incubation with **F3**. After 48 and 72 h, a significant decrease in all conditions was observed, corroborating the suppressor effect of **F3**. These results further demonstrate that the treatment with **F3** maintains a potent effect on cell proliferation and viability in TASK-3 knockdown cells compared to WT and shGFP controls, indicating that the absence of TASK-3 does not afford protection against **F3** that must therefore be acting on TASK-1.

Computational Studies. It has been previously described that bisamidated compounds considered to design **F1−F8** compounds have a common pharmacophore.[21,29] Also, the binding site and binding mode of A1899 in the central cavity of the TASK-1 channel have been described using experimental alanine mutagenesis screens, molecular docking, and molecular dynamics simulations.[20,26] We hypothesize that the synthesized compounds, having the same pharmacophore (Figure 1b), also bind in the central cavity of the TASK-1 channel. To identify the difference in the binding mode of compounds **F3** and **F4** (the most active and least active compounds on TASK-1 channels, respectively), molecular docking, binding free energy (ΔG_{bind}) calculations using the MMGBSA method, and molecular dynamics simulations were carried out. Compounds **F1−F8** were chosen for the molecular docking study. ΔG_{bind} calculations were done to identify the interactions between the eight compounds and the TASK-1 channel and to explain their structure−activity relationship.

Figure 8 shows the correlation between the percentage of inhibition and the ΔG_{bind} of the chosen pose of each compound of the molecular docking study. A correlation (R^2) of 0.86 between the experimental and computational results was achieved. **F3** with a $\Delta G_{bind} = -67.66$ kcal/mol on TASK-1 is the most potent inhibitor of the compounds as seen in electrophysiological experiments and the second with better ΔG_{bind}. The pose of the least active compound (**F4**) in TASK-1 has a less favorable ΔG_{bind} (-59.67 kcal/mol). **F3** and **F4** poses were remarkably similar, showing an RMSD (using LigRMSD server[30]) between the common atoms of the two poses of 0.8 Å (Figure 9a−d).

Despite both compounds having a similar binding mode, there is a great difference in the affinity and selectivity between compounds **F3** and **F4** for the TASK-1 channel; therefore, molecular dynamics simulations were carried out to understand
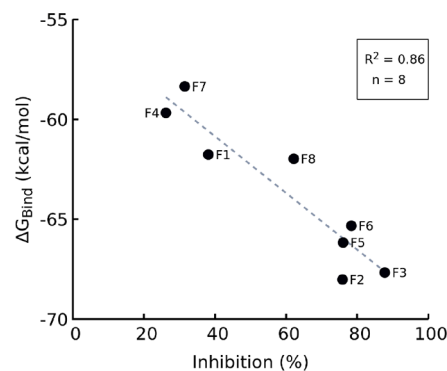

Figure 8. Calculated ΔG_{bind} of compounds **F1−F8** as a function of their observed inhibitory potency expressed as percentage inhibition.

their dynamic behavior and the interactions with TASK-1. Additionally, the highly potent compound BAY1000493 (BAY) ($IC_{50} = 9.5$ nM) crystallized with the TASK-1 channel[23] was also considered to perform the MD simulation and to compare it with compounds **F3** and **F4**.

Figure 10 shows the interaction fractions of compounds **F4**, **F3**, and BAY over 300 ns of MD simulation. The three compounds were stable over time, maintaining a similar orientation to that initially obtained by molecular docking (**F3** and **F4**) and to the crystallographic pose for BAY (Figure S4a). The main change with respect to the initial poses was presented in the BAY compound, which turned the biphenyl ring toward the intracellular side. The rest of the molecule remained in the same crystal orientation (Figure S4c). Regarding the protein stability, TASK-1 during the MD with the different compounds showed a stable behavior over time (Figure S4b). All three compounds show mostly hydrophobic interactions, and compounds **F3** and **F4** show two hydrogen-bond interactions with Q126 residues of both chains that are conserved for ~65−80% of the simulation. Residue Q126 is part of the A293 binding site that also binds to the central cavity of the TASK-1 channel.[21] **F3** and **F4** interact with almost the same residues, and only **F4** presents additional interactions with residues T93, T198, and T199 (water-bridge interactions) and hydrophobic interaction with V243. **F3** presents a hydrophobic interaction with residue I118 that is not present in **F4**. The BAY compound exhibits almost exclusively hydrophobic interactions and a water-bridge interaction with residue L232. Compound **F4** has four water-bridge interactions, while **F3** and BAY have only one interaction. The BAY compound is more potent than **F3** and **F4** compounds, but interestingly, BAY shows fewer interactions than **F3** and **F4**.

F4 establishes interactions with eight residues that make up the binding site of A1899 in the central cavity of the TASK-1 channel[20] (T93, L122, T198, T199, I235, L239, V243, and M247), and **F3** establishes interactions with five residues (I118, L122, I235, L239, and M247). The binding site of **F3** was tested using site-directed mutagenesis, and all the mentioned residues are included in the binding site except M247. In addition, three residues that belong to the **F3** binding site but not the A1899 binding site were reported (F125, Q126, and L232) (Figure 11).

The residues that were mutated to verify the binding site of compound **F3** (Figure 11) were considered to calculate the percentage identity between TASK-1 and the different K_{2P} channels using the multiple alignment reported by Brohawn et al.[31] (Table 2). The percentage identity of the binding site residues between TASK-1 and TRAAK, TREK-1, and TREK-2
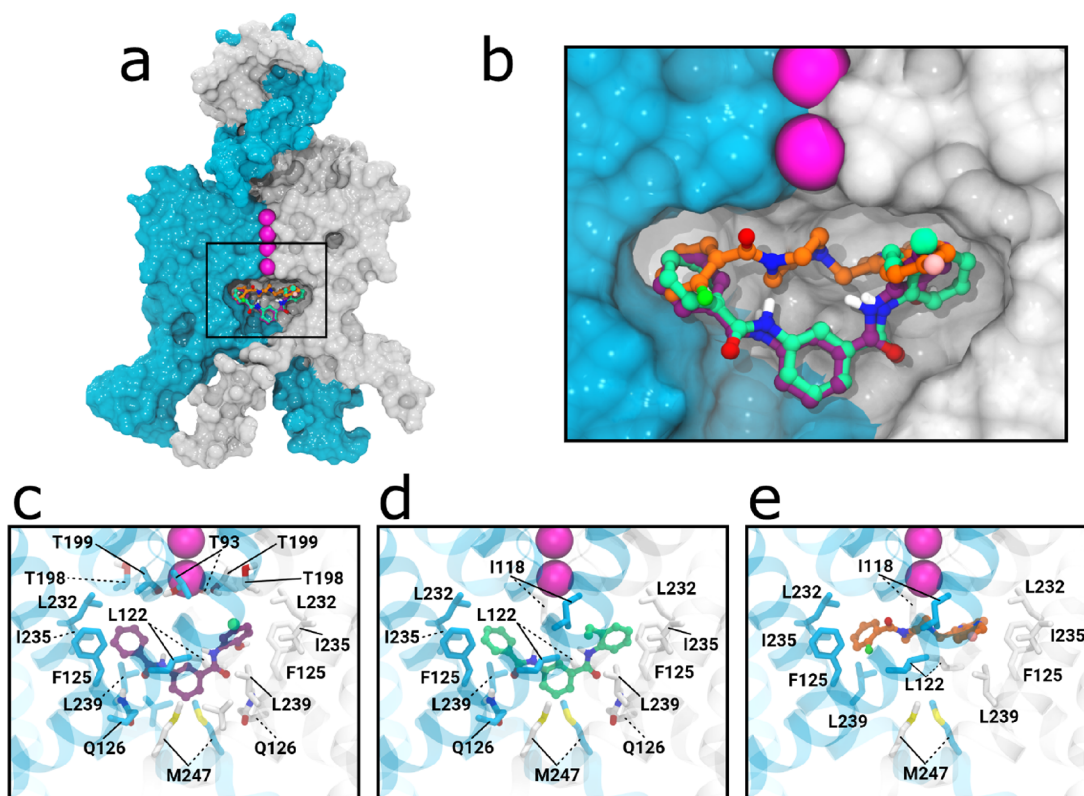
Figure 9. Proposed binding modes for **F3**, **F4**, and crystallographic pose of BAY1000493. (a, b) Overlap between the binding modes of **F4** (purple), **F3** (green), and BAY1000493 (orange). (c−e) Binding sites of compounds **F4**, **F3**, and BAY1000493, respectively, with the residues that showed interactions during the molecular dynamics simulations.
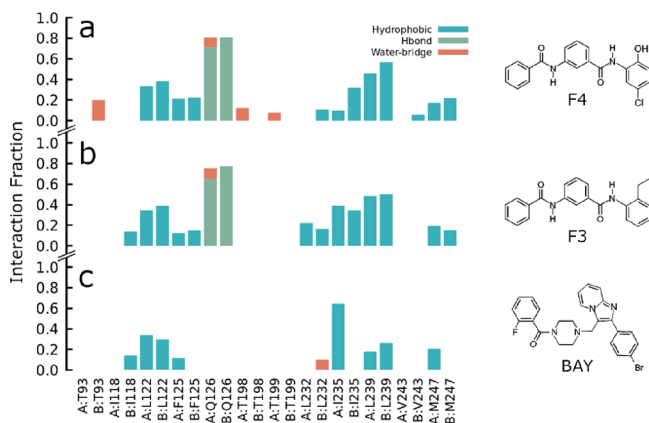

Figure 10. Interaction fractions during 300 ns of molecular dynamics simulations. Only the residues that presented a percentage of interaction greater than 5% during 300 ns of molecular dynamics simulations are shown. (a−c) Interaction fractions of **F4**, **F3**, and BAY compounds, respectively.

Figure 11. Verification of the binding mode of compound **F3** in *Xenopus* oocytes via voltage-clamp recordings. Analysis of inhibition after 2 μM **F3** application for wild-type TASK-1 channels and binding site mutants. All data are presented as the mean $\pm$ SEM. The number of biological replicates (n) is illustrated in the respective bar graphs. *$p <$ 0.05, **$p <$ 0.01, ***$p <$ 0.001.

is 42.86%, whereas for TALK-2 (TASK-4) and THIK-1, it is 28.57% and, for TRESK, it is 14.29%. However, between TASK-1 and TASK-3, the percentage of identity is 100%.

Next, we analyzed how the hydration of the central cavity is affected by the presence of the compounds (Figure S5) and it was found that the three compounds produce similar dehydration compared to the APO system. The APO system has an average of 28 water molecules, while **F4**, **F3**, and BAY systems have 10, 11, and 9, respectively. In this case, the interactions presented by compounds and the number of water molecules in the central cavity do not allow us to establish a direct relationship with their activity.

To study the physicochemical differences between the three compounds, the SiteMap module of the Schrödinger suite was used. SiteMap software is useful for identifying and analyzing molecule binding sites and for predicting druggability.[32,33]

Figure 12 shows the druggability score (Dscore) and the descriptor "balance", which is the relationship between hydrophobicity and the hydrophilicity of the site. It is observed that the druggability score allows establishing a qualitative relationship with the activity of the ligand. The least active ligand (**F4**) has the lowest score, followed by compound **F3** and, last, the most potent compound (BAY). Among the descriptors, the

Table 2. Alignment of the F3 Binding Site Sequence

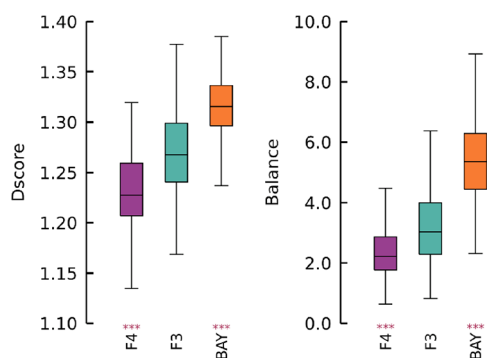| channel	alignment	identity (%)
TASK-1	ILFQLIL	100.00
TASK-3	ILFQLIL	
TASK-1	ILFQLIL	42.86
TRAAK	IGLALFL	
TASK-1	ILFQLIL	42.86
TREK-1	IGLALFL	
TASK-1	ILFQLIL	42.86
TREK-2	IGLALFL	
TASK-1	ILFQLIL	28.57
TALK-2	ILLNMLI	
TASK-1	ILFQLIL	28.57
THIK-1	CIFNVIF	
TASK-1	ILFQLIL	14.29
TRESK	IFLTMVF	

Figure 12. Druggability score and balance. Protein−ligand complexes were selected every 1 ns of 300 ns of MD simulations. The SiteMap module of the Schrödinger suite was used to calculate the druggability score (Dscore) and the balance descriptor. Dscore and Balance were analyzed independently. The significance levels (compared with the **F3** system) are shown as follows: ****$p < 0.0001$, ***$p < 0.001$, **$p < 0.01$, *$p < 0.05$ based on Welch's ANOVA with Games-Howell's post-test.
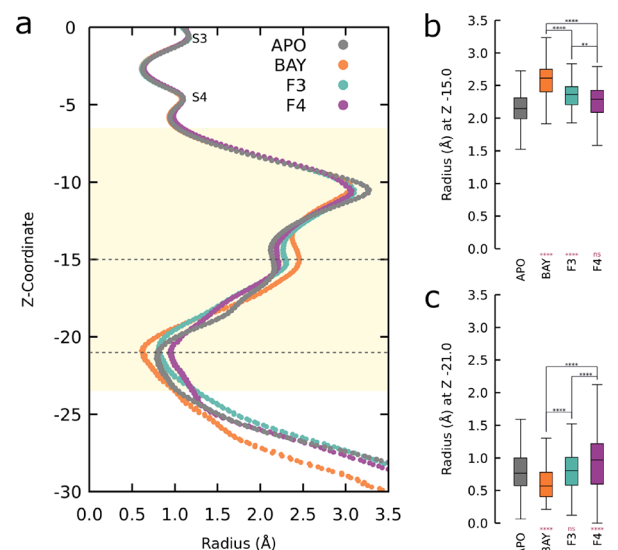
Figure 13. Pore size. Protein structures were selected every 1 ns of 300 ns of MD simulations. The pore radius was measured using HOLE software. (a) The yellow region represents the region of the central cavity. S4 and S3 are the last two occupancy sites of the selectivity filter. (b, c) Boxplot graphs showing the different radii measured in the coordinates z-15 and z-21, respectively. The asterisks at the bottom in red are the comparisons to the apo system. At the top in black, the multiple comparisons between each drug system are shown. The significance levels are shown as follows: ****$p < 0.0001$, ***$p < 0.001$, **$p < 0.01$, *$p < 0.05$ based on Welch's ANOVA with Games-Howell's post-test.

balance was the one that showed the greatest difference, showing that the binding site of compound **F4** is the most hydrophilic with a lower balance, followed by compound **F3** and, last, BAY that presents the most hydrophobic binding site (greater balance).

To study the influence of **F4**, **F3**, and BAY compounds in other structural features of the TASK-1 channel, we measured the root mean square fluctuation (RMSF) of the protein and the pore radius. Regarding RMSF, in general, the most mobile regions of TASK-1 are the extracellular cap, the link between TM2−TM3 segments, the link between P2 and TM4, and the TM4 segment. Particularly, in the region between TM2 and TM3 (residues 147−155) and in the P2−TM4 segment (residues 198−217) of chain A, the TASK-1 channel with the BAY compound showed a greater fluctuation (Figure S6).

To study how the fluctuation in the TM3 and TM4 segments can influence the ion transport mechanism, the pore radius was measured in the 300 frames selected from the previous analyses. Figure 13a shows the average radius of the systems. It is observed that there are two regions of the central cavity with the greatest changes in size at the coordinates −15 and −21 on the z-axis. The studied compounds are mostly located around the −15 z-axis coordinate. In this section, a greater opening of the central cavity is observed for the system with the BAY compound, with

an average value of 2.46 Å, followed by the **F3**, **F4**, and APO systems with values of 2.28, 2.19, and 2.14 Å, respectively (Figure 13b).

The z-21 coordinate is where the x-gate described for the TASK-1 channel is formed, and it is the region where the TM4 segments of each chain are remarkably close. A constriction of the pore is observed that is more marked for the system with the BAY compound, with an average radius value of 0.62 Å, followed by the APO, **F3**, and **F4** systems with values of 0.79, 0.80, and 0.93 Å, respectively. Compound **F4** is the one with the least activity and is the one that generates the least constriction in comparison with compounds **F3** and BAY (Figure 13c). We hypothesize that the interactions of each drug in the central cavity are transmitted to the TM4 helices and generate the bottleneck.

■ DISCUSSION AND CONCLUSIONS

Bisamidated aromatic compounds (specifically **F3**) selectively inhibit, at the submicromolar level, the TASK-1 potassium channel and inhibit the viability of the human breast cancer cells MCF-7. Previously, aromatic amide compounds were described as selective TASK inhibitors. For instance, A1899 showed selectivity for TASK-1 with an IC$_{50}$ of 35 nM (measured in *X. laevis* oocytes) with a 10-fold higher IC$_{50}$ for TASK-3.[20] AVE0118 and S9947 were shown to be 9.6 and 3.5 times more powerful blockers, respectively, against TASK-1 than against the voltage-gated K$^+$ channel Kv1.5. ML365 was identified as a novel selective inhibitor of the TASK-1 potassium channel[22] with an IC$_{50}$ = 16 nM and 62-fold times higher selectivity for TASK-1 than TASK-3.[19] The compound **F3** described here in extent, a derivative from 3-benzamidobenzoic acid, inhibits more TASK-1 than TASK-3 channels with a 12-fold higher IC$_{50}$ for TASK-3.

F3 design was performed rationally, and it is the most active compound of a series of 30 derivatives based on benzamidobenzoic acid against the TASK-1 channel. The rational design was done using homology models of TASK-1 and TASK-3. Nowadays, a crystal structure of the TASK-1 channel is available[23] and is used for subsequent docking and molecular dynamics simulations of **F1–F8** and BAY compounds in this work. However, considering the limitations that we have when we initially designed the benzamidobenzoic acid derivatives, in the absence of a TASK crystal structure, we consider that the rational design based on TASK homology models was a successful strategy to find new TASK blockers, and we suggest this methodology when no experimental structures are available for target proteins.[34]

Regarding the **F3** effect in breast cancer cells, this is the first report of the TASK-1 relevance in the non-invasive breast cancer cell line (MCF-7). Previously, Williams *et al.*[6] observed a high expression of the *KCNK3* gene but in an invasive cancer cell line. In the future, the specific antiproliferative activity of **F3** in MCF-7 must be assayed by comparing against nontumorigenic cells. It will also be relevant to precisely elucidate the mechanism of inhibition of cancer cell proliferation using **F3**.

The binding site of the compound with greater activity (*i.e.*, **F3**) in TASK-1 has been addressed here in a detailed manner. The hydrophobicity of the binding site can explain the difference in the blocking capacity of **F3** and **F4** on TASK-1. Hydrophobic interactions are the most common type of interaction found in ligand–protein crystals and are also more frequent in highly efficient ligands.[35] It has been described that druggable sites can be differentiated from nondruggable sites mainly by their hydrophobicity. Nondruggable sites are highly hydrophilic, while druggable sites are hydrophobic and not remarkably hydrophilic.[33] In addition to the hydrophobicity calculated at the binding site, the compounds BAY, **F3**, and **F4** have predicted consensus values of log $P_{o/w}$ of 4.31, 3.92, and 3.52, respectively,[36] which show a trend between the hydrophobicity of these compounds and their activity. Mechanistically, the bottleneck produced in the central cavity at the *x*-gate could partially explain the activity of the compounds since this bottleneck is qualitatively and inversely proportional to the activity of the compounds. The bottleneck could be an important factor as the larger the bottleneck, the less likely the ions are to enter the pore and pass through the channel. The *x*-gate is responsible for highly selective inhibitors such as BAY1000493 and BAY2341237 binding to the TASK-1 channel and becoming trapped in the central cavity, producing low washout rates.[23] Although **F3** binding site residues are the same for TASK-1 and TASK-3 and, in general, the central cavity residues are also highly conserved, it has been evidenced that other compounds are more active for TASK-1 than for TASK-3, *e.g.*, A1899, A293, and ML365, and the opposite has also been evidenced, *e.g.*, the compound PK-THPP is more active for TASK-3 than for TASK-1.[37] The reasons behind compounds' selective behavior between TASK-1 and TASK-3 remain unknown, but TASK-3 could not exhibit an *x*-gate bottleneck as TASK-1. However, this hypothesis must be corroborated by solving the structure of the TASK-3 channel. In fact, our results show that the *x*-gate bottleneck besides hydrophobicity at the central cavity can be a determining factor for binding compounds in the TASK-1 channel.

■ EXPERIMENTAL SECTION

Rational Design. We used four homology models of the TASK-1 channel reported by Ramírez *et al.*,[26] and we constructed four homology models of TASK-3. The construction of the TASK-3 models was based on the methodology reported by Ramírez and collaborators[26] using as a template the crystallographic structures of other K_{2P} channels: TRAAK (PDB codes: 4I9W and 3UM7),[38] TREK-2 (PDB code: 4BW5),[39] and TWIK-1 (PDB code: 3UKM).[40] The crystals used show differences in their structures, mainly in the state in which the fenestrations are found,[26,40,41] generating the need to carry out the study on different models. On the other hand, we design 30 derivatives based on a head compound (Figure 1a). All of them were subjected to molecular docking to verify the binding to the channels. The cubic grid that defines the search region in the protein was generated at the putative intracellular binding site of TASK,[20] determining as its center the amino acids Thr92 and Thr198 (of both subunits) and with a size of 30 Å. A total of 2400 poses were obtained, with 10 poses per each compound (30 compounds) in eight homology models (four from TASK-1 and four from TASK-3).

To process and organize the 2400 poses of the ligands obtained with molecular docking in the eight homology models, the clustering of ligands script was used (available at www.schrodinger.com/scripcenter/). This script creates a matrix[42] using a measure of distance by pairs between conformations (poses). This measure corresponds to the quadratic mean deviation (RMSD) between pairs of corresponding atoms following an optimal superposition between them.[43] The RMSD was calculated considering the atoms of the head compound.

General Chemistry Experimental and Analytical Details. Melting points (uncorrected) were measured on an Electrothermal IA9100 melting point apparatus (Stone, Staffs, UK). The reaction progress was monitored by means of thin-layer chromatography using silica gel 60 (Merck, Darmstadt, Germany). All reagents were purchased from either Merck or Sigma Aldrich (St. Louis, MO, USA) and used without further purification.

The ^1H and ^{13}C NMR spectra (400.1 MHz for proton and 100.6 MHz for carbon) were recorded on an AM-400 spectrometer (Bruker, Rheinstetten, Germany) using DMSO-d_6 as a solvent. Tetramethylsilane (TMS) was used as an internal standard. Chemical shifts (δ) and J values are reported in ppm and Hz, respectively, relative to the solvent peak of DMSO-d_6 of 2.5 ppm for protons, and in some cases, we observed a 3.6 ppm peak corresponding to residual water present in the solvent. The solvent peak of DMSO-d_6 is 39.7 ppm for carbon atoms. Signals are designated as follows: s, singlet; d, doublet; t, triplet; q, quartet; dd, doublet of doublets; dt, doublet of triplets; m, multiplet. The IR spectra (KBr pellets, 500–4000 cm^{-1}) were recorded on a NEXUS 670 FT-IR spectrophotometer (Thermo Nicolet, Madison, WI, USA). High-resolution mass spectrometry ESI-MS and ESI-MS/MS analyses were conducted in a high-resolution hybrid quadrupole (Q) and orthogonal time-of-flight (TOF) mass spectrometer (Waters/Micromass Q-TOF micro, Manchester, UK) with a constant nebulizer temperature of 100 °C.

3-Aminobenzoic acid **A** (20 mmol) in ethanol (20 mL) was esterified with SOCl$_2$ (60 mmol), obtaining benzoyl chloride. This was kept under stirring in ethanol at room temperature, obtaining the ethyl ester of 3-aminobenzoic acid **B** (7.4 mmol), which was fused with benzoic acid **C** (8.2 mmol) kept under reflux in DCM (10 mL) and SOCl$_2$ at 60 °C, obtaining 3-ethyl acid benzoylamino benzoic **D** (8.5 mmol). 3-Ethyl acid benzoylamino benzoic **D** in the presence of a mixture of methanol/water (2:1) and LiOH (33.4 mmol) was kept under stirring at room temperature, generating 3-benzoylamino-benzoic acid **E** used as a base for the generation of bisamides.

Compound **E** was used as a basis for the formation of a new amide group, making use of the available acid function through a new amidation reaction previously described,[27] and the use of different amines allowed the generation of structural diversity in the compounds to be obtained (**F1–F8**).

The following compounds were prepared according to the methods reported elsewhere.

Since all compounds are solids, the melting point (mp) range was used as an indicator of purity. A very small temperature range (0.5−1 °C) indicates purity >95%.

3-Benzoylamino-N-(4-fluoro-phenyl)-benzamide (F1). Obtained as an off-white solid; yield: 81%. mp: 251−252 °C. ^{1}H NMR (DMSO-d_6, 400.1 MHz) δ (ppm): 10.46 (s, 1H), 10.34 (s, 1H), 8.33 (s, 1H), 8.02 (t, 3H, J = 6.1 Hz), 7.81 (dd, 2H, J = 8.5−5.2 Hz), 7.70 (d, 1H, J = 7.6 Hz), 7.55 (m, 4H), 7.20 (t, 2H, J = 8.8 Hz). ^{13}C{^{1}H} NMR (DMSO-d_6, 100.6 MHz) δ (ppm): 165.68, 165.48, 159.48, 157.09, 139.36, 135.48, 134.64, 131.73, 128.65, 128.43 (2C), 127.68 (2C), 123.34 (2C), 122.57, 122.19, 122.11, 119.92, 115.30, 115.08. IR (KBr, cm^{-1}): 3308.36, 1647.27, 503.8. HRMS (ESI, m/z): calculated for $C_{20}H_{15}FN_2O_2Na$ [M + Na]$^+$, 357.34; found, 357.7622.

3-Benzoylamino-N-thiazol-2-yl-benzamide (F2). Obtained as an off-white solid; yield: 55%. mp: 219−220 °C. ^{1}H NMR (DMSO-d_6, 400.1 MHz) δ (ppm): 12.64 (s, 1H), 10.47 (s, 1H), 8.49 (s, 1H), 8.00 (d, 3H, J = 5.8 Hz), 7.86 (d, 1H, J = 7.6 Hz), 7.57 (m, 5H), 7.29 (d, 1H, J = 3.5 Hz). ^{13}C{^{1}H} NMR (DMSO-d_6, 100.6 MHz) δ (ppm): 165.71 (3C), 139.45, 134.64, 132.86, 131.75, 128.82, 128.45 (2C), 127.89 (2C), 124.18 (2C), 123.05, 120.38, 113.83. IR (KBr, cm^{-1}): 3311.25, 1676.21, 1534.41. HRMS (ESI, m/z): calculated for $C_{17}H_{13}N_3O_2SNa$ [M + Na]$^+$, 346.37; found, 346.7394.

3-Benzoylamino-N-(2-ethyl-phenyl)-benzamide (F3). Obtained as an off-white solid; yield: 78%. mp: 119−120 °C. ^{1}H NMR (DMSO-d_6, 400.1 MHz) δ (ppm): 10.44 (s, 1H), 9.90 (s, 1H), 8.34 (s, 1H), 8.01 (m, 3H), 7.73 (d, 1H, J = 7.5 Hz), 7.61 (m, 1H), 7.53 (m, 3H), 7.3 (d, 2H, J = 4.0 Hz), 7.24 (d, 2H, J = 3.7 Hz), 2.64 (q, 2H, J = 7.5 Hz), 1.15 (t, 3H, J = 7.9 Hz). ^{13}C{^{1}H} NMR (DMSO-d_6, 100.6 MHz) δ (ppm): 165.79, 165.74, 134.86, 139.40, 135.83, 135.29, 134.70, 131.77, 128.72, 128.57, 128.48 (2C), 128.73 (2C), 127.55, 126.55, 126.08, 123.33, 122.51, 120.12, 24.03, 14.19. IR (KBr, cm^{-1}): 3238.91, 2932.15, 1641.48. HRMS (ESI, m/z): calcd for $C_{22}H_{20}N_2O_2Na$ [M + Na]$^+$, 367.41; found, 367.3012.

3-Benzoylamino-N-(5-chloro-2-hydroxy-phenyl)-benzamide (F4). Obtained as an off-beige solid; yield: 66%. mp: 246−246.5 °C. ^{1}H NMR (DMSO-d_6, 400.1 MHz) δ (ppm): 10.48 (s, 1H), 9.40 (s, 1H), 8.35 (s, 1H), 8.03 (dd, 3H, J = 22.5−7.9 Hz), 7.93 (s, 1H), 7.70 (d, 1H, J = 7.6 Hz), 7.65 (m, 4H), 7.07 (d, 1H, J = 8.6 Hz), 6.94 (d, 1H, J = 8.6 Hz). ^{13}C{^{1}H} NMR (DMSO-d_6, 100.6 MHz) δ (ppm): 165.54, 164.87, 147.49, 139.32, 134.39, 134.45, 131.55, 128.73, 128.24 (2C), 127.51 (2C), 127.04, 124.52, 123.37, 122.27 (2C), 121.96, 119.32, 116.50. IR (KBr, cm^{-1}): 3297.99, 1651.41, 469.98. HRMS (ESI, m/z): calculated for $C_{21}H_{15}ClN_3O_3$[M + H]$^+$, 367.80; found, 367.7828.

3-Benzoylamino-N-(3-hydroxy-pyridin-2-yl)-benzamide (F5). Obtained as an off-yellow solid; yield: 64%. mp: 169−170 °C. ^{1}H NMR (DMSO-d_6, 400.1 MHz) δ (ppm): 10.53 (s, 1H), 10.46 (s, 1H), 9.90 (s, 1H), 8.39 (s, 1H), 8.00 (m, 4H), 7.78 (d, 1H, J = 7.6 Hz), 7.56 (m, 4H), 7.34 (d, 1H, J = 8.0 Hz), 7.22 (m, 1H). ^{13}C{^{1}H} NMR (DMSO-d_6, 100.6 MHz) δ (ppm): 166.32, 166.72, 147.28, 140.35, 139.36, 138.73, 134.67, 134.17, 131.77, 128.70, 128.47 (2C), 127.73 (2C), 124.97, 123.80, 123.08, 123.02, 120.46. IR (KBr, cm^{-1}): 3317.14, 1653.05, 1297.74. HRMS (ESI, m/z): calculated for $C_{19}H_{15}N_3O_3Na$ [M + Na]$^+$, 356.34; found, 356.2509.

3-Benzoylamino-N-(phenylmethyl)-benzamide (F6). Obtained as an off-white solid; yield: 58%. mp: 172−173 °C. ^{1}H NMR (DMSO-d_6, 400.1 MHz) δ (ppm): 10.39 (s, 1H), 9.02 (s, 1H), 8.28 (s, 1H), 7.97 (t, 3H, J = 9.2 Hz), 7.57 (m, 4H), 7.45 (t, 1H, J = 7.9 Hz), 7.33 (s, 4H), 7.25 (d, 1H, J = 3.8 Hz), 4.49 (d, 2H, J = 5.7 Hz). ^{13}C{^{1}H} NMR (DMSO-d_6, 100.6 MHz) δ (ppm): 166.04, 165.40, 139.49, 139.05, 134.87, 134.46, 131.49, 128.35, 128.21 (2C), 128.07 (2C), 127.46 (2C), 127.00 (2C), 126.52, 122.89, 121.96, 119.66, 42.43 (2C). IR (KBr, cm^{-1}): 3299.68, 2911.90, 1635.69. HRMS (ESI, m/z): calculated for $C_{21}H_{18}N_2O_2Na$ [M + Na]$^+$, 353.14; found, 353.3362.

3-Benzoylamino-N-(4-methoxy-phenyl)-benzamide (F7). Obtained as an off-white solid; yield: 60%. mp: 209−210 °C. ^{1}H NMR (DMSO-d_6, 400.1 MHz) δ (ppm): 10.45 (s, 1H), 10.16 (s, 1H), 8.31 (s, 1H), 8.00 (d, 3H, J = 6.8 Hz), 7.68 (d, 3H, J = 8.3 Hz), 7.61 (m, 1H), 7.52 (dt, 3H, J = 16.3−7.6 Hz), 6.93 (d, 3H, J = 8.5 Hz), 3.75 (s, 3H). ^{13}C{^{1}H} NMR (DMSO-d_6, 100.6 MHz) δ (ppm): 165.49, 164.95, 155.37, 139.11, 135.55, 134.47, 132.03, 131.54, 128.41, 128.25 (2C), 127.50 (2C), 122.98, 122.83, 121.77 (2C), 119.73, 113.57 (2C), 54.99. IR (KBr, cm^{-1}): 3300.84, 2832.84, 1645.70. HRMS (ESI, m/z): calculated for $C_{21}H_{18}N_2O_3Na$ [M + Na]$^+$, 369.13; found, 368.2134.

3-Benzoylamino-N-[2-(1H-indol-3-yl)-ethyl]-benzamide (F8). Obtained as an off-ocher solid; yield: 66%. mp: 102−103 °C. ^{1}H NMR (DMSO-d_6, 400.1 MHz) δ (ppm): 10.81 (s, 1H), 10.40 (s, 1H), 8.60 (s, 1H), 8.27 (s, 1H), 7.85 (d, 1H, J = 7.2 Hz), 7.97 (dd, 2H, J = 20.4−7.6 Hz), 7.51 (m, 6H), 7.35 (d, 1H, J = 8.07 Hz), 7.20 (s, 1H); 7.07 (t, 1H, J = 7.3 Hz), 6.99 (t, 1H, J = 7.2 Hz); 3.56 (d, 2H, J = 6.2 Hz); 2.97 (t, 2H, J = 6.9 Hz). ^{13}C{^{1}H} NMR (DMSO-d_6, 100.6 MHz) δ (ppm): 166.03, 165.50, 139.09, 136.10, 135.25, 134.53, 131.54, 128.33, 128.28 (2C), 128.09, 127.52 (2C), 127.13, 122.82, 122.43, 121.96, 120.78, 119.66, 118.31, 118.15, 118.09, 25.02. IR (KBr, cm^{-1}): 3473.31, 2848.23, 1644.37. HRMS (ESI, m/z): calculated for $C_{24}H_{21}N_3O_2Na$ [M + Na]$^+$, 406.16; found, 406.3587.

Oocyte Preparation, cRNA Synthesis, cRNA Injection, and TASK-1 Mutants. Oocytes were obtained from anesthetized *X. laevis* frogs and incubated in OR2 solution containing 82.5 mM NaCl, 2 mM KCl, 1 mM MgCl$_2$, and 5 mM HEPES (pH 7.5) substituted with 2 mg/mL collagenase II (Sigma) to remove residual connective tissue. Then, the oocytes were stored at 18 °C in ND96 supplemented with 50 mg/L gentamycin, 274 mg/L sodium pyruvate, and 88 mg/L theophylline. Human TASK-1 (*KCNK3*, NM_002246) as well as TASK-1 mutants, such as TASK-3 (*KCNK9*, NM_AF212829), TASK-4 (*KCNK17*, NM_AF358910), TRAAK (*KCNK4*, NM_001317090), TREK2 (*KCNK10*, AF385400.1), and TREK-1 (*KCNK2*, NM_001017425.3), Kv1.5, Kv2.1, Kv4.3, Kir2.1, BK, and mouse TRESK (*KCNK18*) channels were subcloned into a pSGEM vector, and cDNA was linearized with NheI. Rat THIK-1 (*KCNK13*, AF287303.1) in pSGEM was linearized with Sfi. cRNA was synthesized with the QuickChange Site-Directed Mutagenesis Kit (Agilent Technologies), following the manufacturer's instructions. hERG in pSP64 was linearized with EcoRI, and cRNA was synthesized with the mMESSAGE mMACHINE SP6 kit (Ambion), following the manufacturer's instructions. The quality of cRNA was tested using gel electrophoresis. Oocytes were each injected with 50 nL of cRNA of each channel.

TASK-1 mutants were performed using the QuickChange Site-Directed Mutagenesis Kit (Agilent Technologies). For the mutagenesis procedure, we followed the manufacturer's instructions.

Two-Electrode Voltage-Clamp Recordings. All two-electrode voltage-clamp recordings were performed at room temperature (20−22 °C) with a TurboTEC 10CD (npi) amplifier and a Digidata1200 Series (Axon Instruments) as an analog/digital converter. Micropipettes were made from borosilicate glass capillaries GB150TF-8P (Science Products) and pulled with a DMZ Universal Puller (Zeitz). Recording pipettes had a resistance of 0.5−1.5 megaohms when filled with 3 M KCl solution.

Recording solution ND96 contained 96 mM NaCl, 2 mM KCl, 1.8 mM CaCl$_2$, 1 mM MgCl$_2$, and 5 mM HEPES (pH 7.5). Blockade was analyzed with voltage steps from a holding potential of −80 mV. A first test pulse to 0 mV of 1 s duration was followed by a repolarizing step to −80 mV for 1 s, directly followed by another 1 s test pulse to +40 mV. The effect of drug application was analyzed by a 0 mV step, whereas a ramp protocol from −150 to 40 mV over 3 s was applied for Kir2.1 channels. hERG channels were measured using a depolarizing step to +60 mV, directly followed by a repolarizing step to −70 mV. The sweep time interval was 10 s for all measurements.

Organic compounds at different concentrations were evaluated on channel currents. IC$_{50}$ values and Hill coefficients were calculated by fitting these concentrations to a Hill plot. Compounds **F2** and **F5** were not possible to apply in higher final concentrations than 10 μM due to solubility problems, and therefore, it was not possible to reach a saturated inhibition, which is crucial to calculate a Hill plot. Nonetheless, to estimate the approximate IC$_{50}$ values and Hill coefficients for these compounds, the maximum inhibition was set to 80% manually. Stability in recordings was monitored prior to the addition of compounds, which were removed from the bath to show recovery.

Data were acquired with Clampex 10 (Molecular Devices) and analyzed with Clampfit 10 (MolecularDevices) and Origin 7 (Origin-Lab Corp.).

MTT Cell Viability Assay. To evaluate the cell viability in response to the compound (**F1−F8**), 5×10^4 MCF-7 cells were seeded in 96-well plates. Then, the cells were subjected to the corresponding pharmacological treatments (at 10 mM) and were kept in culture for 4 days. After this, the cells were treated with 100 μL of the MTT reagent (3-[4,5-dimethylthiazol-2-yl]-2,5 diphenyl tetrazolium bromide, Sigma-Aldrich) per well at a final concentration of 0.5 mg/mL. After an incubation period of 1 h at 37 °C, the MTT medium was removed and replaced with 100 μL of dimethyl sulfoxide (DMSO). Cells were incubated in DMSO at room temperature for 10 min under constant agitation. The absorbance of the DMSO solution was measured at 570 nm with a reference reading at 670 nm.

TASK Silencing by Short Hairpin RNA (shRNA). *Cell Culture.* Human breast adenocarcinoma cells, MCF-7 (ATCC HTB-22TM), were cultured in DMEM/F-12 medium (Invitrogen Life Technologies, Carlsbad, CA, USA) supplemented with gentamicin (25 μg/mL), amphotericin B (25 μg/mL), insulin (10 μg/mL), and 10% (v/v) fetal bovine serum (FBS) (Thermo Fisher Scientific, Waltham, MA, USA). HEK-293T cells, used for the generation of retroviral particles, were cultured in DMEM high glucose medium (Thermo Fisher) supplemented with gentamicin (25 μg/mL), amphotericin B (25 μg/mL), prophylactic Plasmocin (InvivoGen, San Diego, CA, USA), and 10% (v/v) FBS. Cells were maintained at 37 °C, 95% humidity, and 5% CO_2.

Generation of Retroviral Particles and MCF-7 Infection. The retroviral vectors were generated to express a short hairpin RNA (shRNA) against GFP (control) and *KCNK3* and *KCNK9* genes in target cells as previously described by Zúñiga *et al.*[44] Oligo-deoxyribonucleotide sequences shBP9 (sense: 5′-CCG GGC TTC ATC ACG TTG ACT AC-3′; antisense: 5′-AAT TCA AAA AGC TTC ATC ACG TTG ACT AC-3′), shAP3 (sense: 5′-CCG GCC TTC AGC TTC GTC TAC AT-3′; antisense: 5′-AAT TCA AAA ACC TTC AGC TTC GTC TAC AT-3′), shBP3 (sense: 5′-CCG GCT CAT AGC AGG TAG GAC TT-3′; antisense: 5′-AAT TCA AAA ACT CAT AGC AGG TAG GAC TT-3′), and shCP3 (sense: 5′-CCG GTG GCC ACT GAT TCC TTT GA-3′; antisense: 5′-AAT TCA AAA ATG GCC ACT GAT TCC TTT GA-3′) were annealed and subcloned into the vector pMKO.1 puro (a gift from Bob Weinberg, Addgene plasmid #8452). Retroviral particles were generated by transfecting pMKO.1 puro-based constructs and packaging plasmids into HEK-293T cells using Lipofectamine 2000 (Invitrogen) according to the manufacturer's instructions. Prior to viral transduction, MCF-7 cells were cultured until a confluence of 70% was reached. Cells were then infected with retroviral particles carrying shGFP, shBP9, shAP3, shBP3, and shCP3 hairpin sequences. After 3 days, the selection process started with 2 μg/mL puromycin (Thermo Fisher) until a stable selection was achieved.

Immunofluorescence Assay. Wild MCF-7 cells and MCF-7 cells transduced with shRNA against Task-1 were seeded in covers, and at 48 h, they were fixed in 4% paraformaldehyde and then blocked and permeabilized with 2% BSA and 0.1% newt X-100. The primary anti-Task-1 mouse antibody (Santa Cruz) (1: 100) was exposed for 4 h at room temperature in the dark. The 488 anti-mouse secondary antibody (Santa Cruz) (1:300) was exposed for 1 h at room temperature in the dark. All washes were done with 1× PBS for 5 min. Finally, the nuclei were labeled with 1 mg/mL DAPI for 10 min at room temperature in the dark. Finally, the coverslips were put in the middle of mounting on object holders. Indirect fluorescence images were obtained with a 40× objective (microscope BX53, Olympus). The Image J Fiji program, an open-source platform for the analysis of biological images, was used for the analysis and editing of the positive cells. Five independent fields were considered with $n = 3$.

Proliferation and Cell Viability Assays. Cell viability was measured using the trypan blue exclusion method. Confluent cultures of MCF-7 cells under different conditions (wild-type (WT), shGFP, shBP9, shAP3, shBP3, and shCP3) were first trypsinized. Then, 5.5×10^4 cells/mL were seeded in 12-well plates for each condition and in duplicate in the presence or absence of compound **F3** at a concentration of 148 nM

(according to the IC_{50}) or DMSO (compound **F3** is dissolved in DMSO). Cell proliferation and cell viability were determined by measuring the number of total and viable cells with 0.4% trypan blue vital stain (Thermo Scientific). The percentage of trypan blue-negative cells was determined by a LUNA-II Automated Cell Counter (Logos Biosystems, Gyeonggi-do, Korea). Curves for both analyses were determined at 24, 48, and 72 h post seeding in three independent experiments.

Computational Biology. *Molecular Docking.* The human TASK-1 crystallographic structure (PDB code: 6RV3; chains A and B)[23] was used for molecular docking and molecular dynamics simulations. The structure was prepared using the "Protein preparation wizard" module of Schrödinger's suite software (Protein Preparation Wizard; Epik, Schrödinger, LLC, New York, NY, 2018-4; Impact, Schrödinger, LLC, New York, NY, 2018-4; Prime, Schrödinger, LLC, New York, NY, 2018-4). The protonation states of the protein were predicted at a pH of 7.0 with PROPKA.[45] Charges and parameters were assigned according to the force field OPLS-2005.[46] Compounds **F1−F8** were prepared using the LigPrep module in Maestro (LigPrep, Schrödinger, LLC, New York, NY, 2018-4) and docked using Glide v7.4 with standard precision (SP) mode.[47] The grid box was centered in the central cavity of the channel using a cubic box with 25 Å of axial length. Ten poses were generated for each studied ligand, and a rescoring of the poses was performed by calculating the binding free energy using the molecular mechanics−generalized Born surface area (MM-GBSA) method.[48,49]

Molecular Dynamics Simulations. TASK-1 in complex with each ligand (**F3**, **F4**, or BAY1000493 (BAY)) was subjected to molecular dynamics simulations using Desmond v5.7[50] and OPLS-2005 force field.[46] The missing residues in TASK-1 (149−151, chain A; 150−151, chain B) were modeled using the "crosslink protein" tool from the Schrödinger suite. The crystallographic waters, K^+ ions from the selectivity filter (SF), and cholesterol hemisuccinate lipids were kept in the systems. Protein−ligand complexes were embedded into a pre-equilibrated POPC (1-palmitoyl-2-oleoylphosphatidylcholine) bilayer. The systems were solvated using the TIP3P (transferable intermo-lecular potential with 3 points) water model,[51] and chloride ions were added to neutralize the systems. Finally, the ion concentration was set to 0.15 M KCl.

The systems were relaxed using a membrane equilibration protocol consisting of six steps. The first stage consists of a 100 ps Brownian dynamics in an NVT ensemble at 10 K, applying harmonic restrictions on the heavy atoms of the protein, ions of SF, lipids, and ligand (force constant, 50 kcal/mol Å²). The second stage corresponds to a Brownian dynamics of 20 ps in the NPT assembly at 100 K, applying harmonic restrictions to the heavy atoms of the protein and lipids (force constant, 20 kcal/mol Å²), membrane (except for the hydrogen atoms) in the z-direction (force constant 5 kcal/mol Å²), and ions of SF, lipids, and ligand (force constant, 50 kcal/mol Å²). The third stage consisted of a 10 ps simulation in an NPγT (semi-isotropic) ensemble at 100 K, applying restrictions to the heavy atoms of the protein, ions of SF, lipids, and ligand (force constant, 50 kcal/mol Å²) and phosphorus and nitrogen atoms of the membrane in the z-direction (2 kcal/mol Å²). The fourth stage consisted of heating from 100 to 300 K during 150 ps using the same restrictions as the previous step but gradually releasing the restrictions. The fifth stage consisted of a 100 ps simulation in the NVT ensemble, applying a restriction to the protein backbone and heavy atoms of the lipids and ligand (force constant, 50 kcal/mol Å²). Finally, the sixth stage consisted of a simulation of 100 ps in an NPγT assembly at 300 K, applying a restriction to the protein backbone (force constant, 50 kcal/mol Å²).

After a proper membrane equilibration, the complexes were subjected to a second equilibration by 50 ns in NPγT (semi-isotropic ensemble) with positional restraints of 1.0 kcal/mol Å² on the ligand and 0.05 kcal/mol Å² on the protein backbone and cholesterol hemisuccinate lipids. The temperature and pressure were kept constant at 300 K and 1.01325 bar, respectively, by coupling to a Nosé−Hoover chain thermostat[52] and Martyna−Tobias−Klein barostat[53] with an integration time step of 2 fs. Finally, positional restraints were removed, and a molecular dynamics (MD) simulation of 300 ns was performed for each system using an NPγT ensemble. This MD protocol was

applied to the four systems (TASK-1:F3, TASK-1:F4, TASK-1:BAY, and TASK-1 apo).

Druggability Score and Balance Descriptor. The druggability score (Dscore) and balance descriptor (Balance) were calculated in 300 ns of MD simulations of the three non-apo systems: TASK-1 (**F3**, **F4**, or BAY1000493) using the SiteMap[32,33] module from the Schrödinger suite. The data correspond to 300 values for each system (1 complex every 1 ns). Molecules at 10 Å around each ligand were considered. Each site was defined considering the coordinates of the ligand in each frame, with a "sitebox" parameter of 5 Å. The balance descriptor corresponds to a ratio between the hydrophobic (phobic) and hydrophilic (philic) scores of the site. Therefore, the higher the values for the balance descriptor, the more hydrophobic is the binding site where the ligand is found.

Statistical Analysis. Statistical analyses of Figures 5 and 12 and Figure S5 were performed using R software version 3.6.3.[54,55] It was first verified if the data followed a normal distribution, then it was verified if variances were homogeneous, and according to this result, a statistical parametric or nonparametric test was performed.[54,55] The Anderson−Darling,[56] Lilliefors[57] (Kolmogorov−Smirnov), Jarque−Bera,[58] and Shapiro−Wilk[59] tests were used to verify the normality condition based on data type. The homogeneity of variances was verified with Levene's test.[60] The parametric tests used were ANOVA and two-way ANOVA. The nonparametric tests used were Kruskal−Wallis[61] with a post hoc analysis using the Nemenyi test[62] and Welch's ANOVA[54] test with a post hoc analysis using the Games-Howell test.[63] The significance levels in each test are described in each plot.

Statistical analyses of Figures 6 and 7 were performed using GraphPad Prism (version 7.0, San Diego, CA, USA). Group differences were calculated with two-way ANOVA with Tukey's post-test analysis. Significant values were all those with $p \leq 0.05$. Results were represented as the mean ± SEM of three independent experiments.

■ ASSOCIATED CONTENT

ⓈⒾ Supporting Information

The Supporting Information is available free of charge at https://pubs.acs.org/doi/10.1021/acs.jmedchem.1c00378.

> Molecular formula strings (CSV)
>
> PDB coordinates for docked complexes of TASK-1 (PDB code: 6RV3) and compounds BAY, **F3**, and **F4** (ZIP)
>
> Compounds selected to be synthesized; levels of Task-1 expression; Task-1 channel immunofluorescence; effect of knocking down TASK-1 on MCF-7 cell proliferation and viability; behavior of the systems during MD simulation; central cavity hydration; protein RMSF; additional figures, details of the NMR spectra (PDF)

■ AUTHOR INFORMATION

Corresponding Authors

Leandro Zúñiga − *Centro de Nanomedicina, Diagnóstico y Desarrollo de Fármacos (ND3), Laboratorio de Fisiología Molecular, Escuela de Medicina, Universidad de Talca, 3460000 Talca, Chile;* Email: wgonzalez@utalca.cl

Margarita Gutierrez − *Laboratorio de Síntesis y Actividad Biológica, Instituto de Química de Recursos Naturales, Universidad de Talca, 3460000 Talca, Chile;* Email: mgutierrez@utalca.cl

Wendy González − *Centro de Bioinformática, Simulación y Modelado (CBSM), Facultad de Ingeniería and Millennium Nucleus of Ion Channels-Associated Diseases (MiNICAD), Universidad de Talca, 3460000 Talca, Chile;* ⓄRCID.org/ 0000-0002-7535-6883; Email: lzuniga@utalca.cl

Niels Decher − *Institute for Physiology and Pathophysiology, Vegetative Physiology, Philipps-University of Marburg, 35037 Marburg, Germany; Marburg Center for Mind, Brain and Behavior−MCMBB, Philipps-University Marburg, 35037 Marburg, Germany;* Email: decher@staff.uni-marburg.de

Authors

Bárbara Arévalo − *Centro de Estudios en Alimentos Procesados−CEAP, 3460000 Talca, Chile*

Mauricio Bedoya − *Centro de Investigación de Estudios Avanzados del Maule (CIEAM), Vicerrectoría de Investigación y Postgrado, Universidad Católica del Maule, 3460000 Talca, Chile; Laboratorio de Bioinformática y Química Computacional, Departamento de Medicina Traslacional, Facultad de Medicina, Universidad Católica del Maule, 3480094 Talca, Chile;* ⓄRCID.org/0000-0002-3542-7528

Aytug K. Kiper − *Institute for Physiology and Pathophysiology, Vegetative Physiology, Philipps-University of Marburg, 35037 Marburg, Germany;* ⓄRCID.org/0000-0003-2850-2523

Fernando Vergara − *Centro de Bioinformática, Simulación y Modelado (CBSM), Facultad de Ingeniería, Universidad de Talca, 3460000 Talca, Chile*

David Ramírez − *Departamento de Farmacología, Facultad de Ciencias Biológicas, Universidad de Concepción, 4030000 Concepción, Chile*

Yuliet Mazola − *Centro de Bioinformática, Simulación y Modelado (CBSM), Facultad de Ingeniería, Universidad de Talca, 3460000 Talca, Chile*

Daniel Bustos − *Centro de Investigación de Estudios Avanzados del Maule (CIEAM), Vicerrectoría de Investigación y Postgrado and Laboratorio de Bioinformática y Química Computacional (LBQC), Escuela de Química y Farmacia, Facultad de Medicina, Universidad Católica del Maule, 3460000 Talca, Chile*

Rafael Zúñiga − *Centro de Nanomedicina, Diagnóstico y Desarrollo de Fármacos (ND3), Laboratorio de Fisiología Molecular, Escuela de Medicina and Instituto de Investigación Interdisciplinaria, Vicerrectoría Académica, Universidad de Talca, 3460000 Talca, Chile*

Rocio Cikutovic − *Centro de Nanomedicina, Diagnóstico y Desarrollo de Fármacos (ND3), Laboratorio de Fisiología Molecular, Escuela de Medicina, Universidad de Talca, 3460000 Talca, Chile*

Angel Cayo − *Centro de Nanomedicina, Diagnóstico y Desarrollo de Fármacos (ND3), Laboratorio de Fisiología Molecular, Escuela de Medicina, Universidad de Talca, 3460000 Talca, Chile*

Susanne Rinné − *Institute for Physiology and Pathophysiology, Vegetative Physiology, Philipps-University of Marburg, 35037 Marburg, Germany*

M. Teresa Ramirez-Apan − *Instituto de Química, Universidad Nacional Autónoma de México, 04510 México, DF, México*

Francisco V. Sepúlveda − *Centro de Estudios Científicos (CECs), 5110466 Valdivia, Chile; Facultad de Medicina y Ciencia, Universidad San Sebastián, 5110466 Valdivia, Chile*

Oscar Cerda − *Programa de Biología Celular y Molecular, Instituto de Ciencias Biomédicas (ICBM), Facultad de Medicina and Millennium Nucleus of Ion Channels-Associated Diseases (MiNICAD), Facultad de Medicina, Universidad de Chile, 8380453 Santiago, Chile*

Eduardo López-Collazo − *The Innate Immune Response Group and Tumor Immunology Laboratory, IdiPAZ, La Paz University Hospital, 8046 Madrid, Spain*

Complete contact information is available at:
https://pubs.acs.org/10.1021/acs.jmedchem.1c00378

Author Contributions

∞B.A., M.B., and A.K.K. contributed equally to this work.

Author Contributions

The manuscript was written with contributions of all authors. All authors approved the final version of the manuscript.

Notes

The authors declare no competing financial interest.

■ ABBREVIATIONS

CHO, Chinese hamster ovary; DMSO-d_6, dimethyl sulfoxide deuterated; Dscore, druggability score; EMT, epithelial—mesenchymal transition; K_{2P}, two-pore domain K$^+$ channels; MCF-7, breast cancer cell line (Michigan Cancer Foundation-7); mp, melting point; NSCLC, non-small-cell lung cancer; OVCAR-3, Ovarian Carcinoma Cells; P1, first pore domain; P2, second pore domain; S1—S4, transmembrane domains S1, S2, S3, and S4; SF, selectivity filter; shRNA, short hairpin RNA; SKOV-2, human ovarian cancer cell line; TASK, Twik-related acid-sensitive K$^+$ channel; TALK, Twik-related alkaline pH-activated K$^+$ channel; TEVC, two-electrode voltage clamp; THIK, tandem pore domain halothane-inhibited K$^+$ channel; TREK, Twik-related K$^+$ channel; TRESK, Twik-related spinal cord K$^+$ channel; TWIK, tandem of pore domains in weak inward rectifying K$^+$ channel; *X.* oocytes, *X. laevis* oocytes

■ REFERENCES

(1) Lesage, F.; Lazdunski, M. Molecular and Functional Properties of Two-Pore-Domain Potassium Channels. *Am. J. Physiol.: Renal, Fluid Electrolyte Physiol.* **2000**, *279*, F793—F801.

(2) Comes, N.; Serrano-Albarrás, A.; Capera, J.; Serrano-Novillo, C.; Condom, E.; Ramón y Cajal, S.; Ferreres, J. C.; Felipe, A. Involvement of Potassium Channels in the Progression of Cancer to a More Malignant Phenotype. *Biochim. Biophys. Acta, Biomembr.* **2015**, *1848*, 2477—2492.

(3) Goldstein, S. A. N.; Bockenhauer, D.; O'Kelly, I.; Zilberberg, N. Potassium Leak Channels and the KCNK Family of Two-P-Domain Subunits. *Nat. Rev. Neurosci.* **2001**, *2*, 175—184.

(4) Czirják, G.; Enyedi, P. Formation of Functional Heterodimers between the TASK-1 and TASK-3 Two-Pore Domain Potassium Channel Subunits. *J. Biol. Chem.* **2002**, *277*, 5426—5432.

(5) Villalonga, N.; Ferrere, J. C.; Argiles, J. M.; Felipe, E. C. *Potassium Channels are a New Target Field in Anticancer Drug Design*; Recent Patents on Anti-Cancer Drug Discovery. https://www.eurekaselect.com/81858/article (accessed 2020—11—23), 2007.

(6) Williams, S.; Bateman, A.; O'Kelly, I. Altered Expression of Two-Pore Domain Potassium (K_{2P}) Channels in Cancer. *PLoS One* **2013**, *8*, No. e74589.

(7) Kim, Y.; Bang, H.; Kim, D. TASK-3, a New Member of the Tandem Pore K(+) Channel Family. *J. Biol. Chem.* **2000**, *275*, 9340—9347.

(8) Rajan, S.; Wischmeyer, E.; Xin Liu, G.; Preisig-Müller, R.; Daut, J.; Karschin, A.; Derst, C. TASK-3, a Novel Tandem Pore Domain Acid-Sensitive K+ Channel. An Extracellular Histidin as PH Sensor. *J. Biol. Chem.* **2000**, *275*, 16650—16657.

(9) Pei, L.; Wiser, O.; Slavin, A.; Mu, D.; Powers, S.; Jan, L. Y.; Hoey, T. Oncogenic Potential of TASK3 (Kcnk9) Depends on K+ Channel Function. *Proc. Natl. Acad. Sci. U. S. A.* **2003**, *100*, 7803—7807.

(10) Mu, D.; Chen, L.; Zhang, X.; See, L.-H.; Koch, C. M.; Yen, C.; Tong, J. J.; Spiegel, L.; Nguyen, K. C. Q.; Servoss, A.; Peng, Y.; Pei, L.; Marks, J. R.; Lowe, S.; Hoey, T.; Jan, L. Y.; McCombie, W. R.; Wigler, M. H.; Powers, S. Genomic Amplification and Oncogenic Properties of the KCNK9 Potassium Channel Gene. *Cancer Cell* **2003**, *3*, 297—302.

(11) Pocsai, K.; Kosztka, L.; Bakondi, G.; Gönczi, M.; Fodor, J.; Dienes, B.; Szentesi, P.; Kovács, I.; Feniger-Barish, R.; Kopf, E.; Zharhary, D.; Szűcs, G.; Csernoch, L.; Rusznák, Z. Melanoma Cells Exhibit Strong Intracellular TASK-3-Specific Immunopositivity in Both Tissue Sections and Cell Culture. *Cell. Mol. Life Sci.* **2006**, *63*, 2364—2376.

(12) Innamaa, A.; Jackson, L.; Asher, V.; Van Shalkwyk, G.; Warren, A.; Hay, D.; Bali, A.; Sowter, H.; Khan, R. Expression and Prognostic Significance of the Oncogenic K2P Potassium Channel KCNK9 (TASK-3) in Ovarian Carcinoma. *Anticancer Res.* **2013**, *33*, 1401—1408.

(13) Cikutović-Molina, R.; Herrada, A. A.; González, W.; Brown, N.; Zúñiga, L. TASK-3 Gene Knockdown Dampens Invasion and Migration and Promotes Apoptosis in KATO III and MKN-45 Human Gastric Adenocarcinoma Cell Lines. *Int. J. Mol. Sci.* **2019**, *20*, 6077.

(14) Kim, C. J.; Cho, Y. G.; Jeong, S. W.; Kim, Y. S.; Kim, S. Y.; Nam, S. W.; Lee, S. H.; Yoo, N. J.; Lee, J. Y.; Park, W. S. Altered Expression of KCNK9 in Colorectal Cancers. *APMIS* **2004**, *112*, 588—594.

(15) Wang, X.-G.; Yuan, N.-X.; Li, X.-P.; Chen, F.-F. TASK-1 Induces Gefitinib Resistance by Promoting Cancer Initiating Cell Formation and Epithelial-Mesenchymal Transition in Lung Cancer. *Exp. Ther. Med.* **2018**, *15*, 365—370.

(16) Duprat, F.; Lesage, F.; Fink, M.; Reyes, R.; Heurteaux, C.; Lazdunski, M. TASK, a Human Background K+ Channel to Sense External PH Variations near Physiological PH. *EMBO J.* **1997**, *16*, 5464—5471.

(17) Leithner, K.; Hirschmugl, B.; Li, Y.; Tang, B.; Papp, R.; Nagaraj, C.; Stacher, E.; Stiegler, P.; Lindenmann, J.; Olschewski, A.; Olschewski, H.; Hrzenjak, A. TASK-1 Regulates Apoptosis and Proliferation in a Subset of Non-Small Cell Lung Cancers. *PLoS One* **2016**, *11*, No. e0157453.

(18) Oskarsson, T. Extracellular Matrix Components in Breast Cancer Progression and Metastasis. *Breast* **2013**, *22*, S66—S72.

(19) Flaherty, D. P.; Simpson, D. S.; Miller, M.; Maki, B. E.; Zou, B.; Shi, J.; Wu, M.; McManus, O. B.; Aubé, J.; Li, M.; Golden, J. E. Potent and Selective Inhibitors of the TASK-1 Potassium Channel through Chemical Optimization of a Bis-Amide Scaffold. *Bioorg. Med. Chem. Lett.* **2014**, *24*, 3968—3973.

(20) Streit, A. K.; Netter, M. F.; Kempf, F.; Walecki, M.; Rinné, S.; Bollepalli, M. K.; Preisig-Müller, R.; Renigunta, V.; Daut, J.; Baukrowitz, T.; Sansom, M. S. P.; Stansfeld, P. J.; Decher, N. A Specific Two-Pore Domain Potassium Channel Blocker Defines the Structure of the TASK-1 Open Pore. *J. Biol. Chem.* **2011**, *286*, 13977—13984.

(21) Kiper, A. K.; Rinné, S.; Rolfes, C.; Ramírez, D.; Seebohm, G.; Netter, M. F.; González, W.; Decher, N. Kv1.5 Blockers Preferentially Inhibit TASK-1 Channels: TASK-1 as a Target against Atrial Fibrillation and Obstructive Sleep Apnea? *Pflugers Arch.* **2015**, *467*, 1081—1090.

(22) Zou, B.; Flaherty, D. P.; Simpson, D. S.; Maki, B. E.; Miller, M. R.; Shi, J.; Wu, M.; McManus, O. B.; Golden, J. E.; Aubé, J.; Li, M. *ML365: Development of Bis-Amides as Selective Inhibitors of the KCNK3/TASK1 Two Pore Potassium Channel*; National Center for Biotechnology Information (US), 2013.

(23) Rödström, K. E. J.; Kiper, A. K.; Zhang, W.; Rinné, S.; Pike, A. C. W.; Goldstein, M.; Conrad, L. J.; Delbeck, M.; Hahn, M. G.; Meier, H.; Platzk, M.; Quigley, A.; Speedman, D.; Shrestha, L.; Mukhopadhyay, S.

M. M.; Burgess-Brown, N. A.; Tucker, S. J.; Müller, T.; Decher, N.; Carpenter, E. P. A Lower X-Gate in TASK Channels Traps Inhibitors within the Vestibule. *Nature* **2020**, *582*, 443−447.

(24) Lee, G.-W.; Park, H. s.; Kim, E.-J.; Cho, Y.-W.; Kim, G.-T.; Mun, Y.-J.; Choi, E.-J.; Lee, J.-S.; Han, J.; Kang, D. Reduction of Breast Cancer Cell Migration via Up-Regulation of TASK-3 Two-Pore Domain K + Channel. *Acta Physiol.* **2012**, *204*, 513−524.

(25) Zúñiga, R.; Valenzuela, C.; Concha, G.; Brown, N.; Zúñiga, L. TASK-3 Downregulation Triggers Cellular Senescence and Growth Inhibition in Breast Cancer Cell Lines. *Int. J. Mol. Sci.* **2018**, *19*, 1033.

(26) Ramírez, D.; Arévalo, B.; Martínez, G.; Rinné, S.; Sepúlveda, F. V.; Decher, N.; González, W. Side Fenestrations Provide an "Anchor" for a Stable Binding of A1899 to the Pore of TASK-1 Potassium Channels. *Mol. Pharmaceutics* **2017**, 2197.

(27) Hosangadi, B. D.; Dave, R. H. An Efficient General Method for Esterification of Aromatic Carboxylic Acids. *Tetrahedron Lett.* **1996**, *37*, 6375−6378.

(28) Ferrari, M.; Fornasiero, M. C.; Isetta, A. M. MTT Colorimetric Assay for Testing Macrophage Cytotoxic Activity in Vitro. *J. Immunol. Methods* **1990**, *131*, 165−172.

(29) Bedoya, M.; Rinné, S.; Kiper, A. K.; Decher, N.; González, W.; Ramírez, D. TASK Channels Pharmacology: New Challenges in Drug Design. *J. Med. Chem.* **2019**, 10044.

(30) Velázquez-Libera, J. L.; Durán-Verdugo, F.; Valdés-Jiménez, A.; Núñez-Vivanco, G.; Caballero, J. LigRMSD: A Web Server for Automatic Structure Matching and RMSD Calculations among Identical and Similar Compounds in Protein-Ligand Docking. *Bioinformatics* **2020**, *36*, 2912−2914.

(31) Brohawn, S. G.; del Mármol, J.; MacKinnon, R. Crystal Structure of the Human K2P TRAAK, a Lipid- and Mechano-Sensitive K+ Ion Channel. *Science* **2012**, *335*, 436−441.

(32) Halgren, T. New Method for Fast and Accurate Binding-Site Identification and Analysis. *Chem. Biol. Drug Des.* **2007**, *69*, 146−148.

(33) Halgren, T. A. Identifying and Characterizing Binding Sites and Assessing Druggability. *J. Chem. Inf. Model.* **2009**, *49*, 377−389.

(34) Ramírez, D.; Concha, G.; Arévalo, B.; Prent-Peñaloza, L.; Zúñiga, L.; Kiper, A. K.; Rinné, S.; Reyes-Parada, M.; Decher, N.; González, W.; Caballero, J. Discovery of Novel TASK-3 Channel Blockers Using a Pharmacophore-Based Virtual Screening. *Int. J. Mol. Sci.* **2019**, *20*, 4014.

(35) Ferreira de Freitas, R.; Schapira, M. A Systematic Analysis of Atomic Protein-Ligand Interactions in the PDB. *MedChemComm* **2017**, *8*, 1970−1981.

(36) Daina, A.; Michielin, O.; Zoete, V. SwissADME: A Free Web Tool to Evaluate Pharmacokinetics, Drug-Likeness and Medicinal Chemistry Friendliness of Small Molecules. *Sci. Rep.* **2017**, *7*, 42717.

(37) Decher, N.; Rinné, S.; Bedoya, M.; Gonzalez, W.; Kiper, A. K. Molecular Pharmacology of K2P Potassium Channels | Cell Physiol Biochem. *Cell. Physiol. Biochem.* **2021**, *55*, 87−107.

(38) Brohawn, S. G.; Campbell, E. B.; MacKinnon, R. Domain-Swapped Chain Connectivity and Gated Membrane Access in a Fab-Mediated Crystal of the Human TRAAK K+ Channel. *Proc. Natl. Acad. Sci. U. S. A.* **2013**, *110*, 2129−2134.

(39) Dong, Y. Y.; Pike, A. C. W.; Mackenzie, A.; McClenaghan, C.; Aryal, P.; Dong, L.; Quigley, A.; Grieben, M.; Goubin, S.; Mukhopadhyay, S.; Ruda, G. F.; Clausen, M. V.; Cao, L.; Brennan, P. E.; Burgess-Brown, N. A.; Sansom, M. S. P.; Tucker, S. J.; Carpenter, E. P. K2P Channel Gating Mechanisms Revealed by Structures of TREK-2 and a Complex with Prozac. *Science* **2015**, *347*, 1256−1259.

(40) Miller, A. N.; Long, S. B. Crystal Structure of the Human Two-Pore Domain Potassium Channel K2P1. *Science* **2012**, *335*, 432−436.

(41) Aryal, P.; Abd-Wahab, F.; Bucci, G.; Sansom, M. S. P.; Tucker, S. J. A Hydrophobic Barrier Deep within the Inner Pore of the TWIK-1 K2P Potassium Channel. *Nat. Commun.* **2014**, *5*, 4377.

(42) Lorenzen, S.; Zhang, Y. Identification of Near-Native Structures by Clustering Protein Docking Conformations. *Proteins* **2007**, *68*, 187−194.

(43) Shenkin, P. S.; McDonald, D. Q. Cluster Analysis of Molecular Conformations. *J. Comput. Chem.* **2004**, *15*, 899−916.

(44) Zúñiga, R.; Concha, G.; Cayo, A.; Cikutović-Molina, R.; Arevalo, B.; González, W.; Catalán, M. A.; Zúñiga, L. Withaferin A Suppresses Breast Cancer Cell Proliferation by Inhibition of the Two-Pore Domain Potassium (K2P9) Channel TASK-3. *Biomed. Pharmacother.* **2020**, *129*, No. 110383.

(45) Olsson, M. H. M.; Søndergaard, C. R.; Rostkowski, M.; Jensen, J. H. PROPKA3: Consistent Treatment of Internal and Surface Residues in Empirical PKa Predictions. *J. Chem. Theory Comput.* **2011**, *7*, 525−537.

(46) Kaminski, G. A.; Friesner, R. A.; Tirado-Rives, J.; Jorgensen, W. L. Evaluation and Reparametrization of the OPLS-AA Force Field for Proteins via Comparison with Accurate Quantum Chemical Calculations on Peptides. *J. Phys. Chem. B* **2001**, *105*, 6474−6487.

(47) Friesner, R. A.; Banks, J. L.; Murphy, R. B.; Halgren, T. A.; Klicic, J. J.; Mainz, D. T.; Repasky, M. P.; Knoll, E. H.; Shelley, M.; Perry, J. K.; Shaw, D. E.; Francis, P.; Shenkin, P. S. Glide: A New Approach for Rapid, Accurate Docking and Scoring. 1. Method and Assessment of Docking Accuracy. *J. Med. Chem.* **2004**, *47*, 1739−1749.

(48) Gohlke, H.; Case, D. A. Converging free energy estimates: MM-PB(GB)SA studies on the protein−protein complex Ras−Raf. *J. Comput. Chem.* **2004**, *25*, 238−250.

(49) Hou, T.; Wang, J.; Li, Y.; Wang, W. Assessing the Performance of the MM/PBSA and MM/GBSA Methods. 1. The Accuracy of Binding Free Energy Calculations Based on Molecular Dynamics Simulations. *J. Chem. Inf. Model.* **2011**, *51*, 69−82.

(50) Bowers, K. J.; Chow, D. E.; Xu, H.; Dror, R. O.; Eastwood, M. P.; Gregersen, B. A.; Klepeis, J. L.; Kolossvary, I.; Moraes, M. A.; Sacerdoti, F. D.; Salmon, J. K.; Shan, Y.; Shaw, D. E. Scalable Algorithms for Molecular Dynamics Simulations on Commodity Clusters. In *SC '06: Proceedings of the 2006 ACM/IEEE Conference on Supercomputing*; IEEE 2006; pp. 43−43. DOI: 10.1109/SC.2006.54.

(51) Jorgensen, W. L.; Chandrasekhar, J.; Madura, J. D.; Impey, R. W.; Klein, M. L. Comparison of Simple Potential Functions for Simulating Liquid Water. *J. Chem. Phys.* **1983**, *79*, 926−935.

(52) Cheng, A.; Merz, K. M. Application of the Nosé−Hoover Chain Algorithm to the Study of Protein Dynamics. *J. Phys. Chem.* **1996**, *100*, 1927−1937.

(53) Martyna, G. J.; Tobias, D. J.; Klein, M. L. Constant Pressure Molecular Dynamics Algorithms. *J. Chem. Phys.* **1994**, *101*, 4177−4189.

(54) Dag, O.; Dolgun, A.; Konar, N. M. Onewaytests: An R Package for One-Way Tests in Independent Groups Designs. *R J.* **2018**, *10*, 175.

(55) Heumann, C.; Schomaker, M.; Shalabh. *Introduction to Statistics and Data Analysis : With Exercises, Solutions and Applications in R*; Springer International Publishing, 2016. DOI: 10.1007/978-3-319-46162-5.

(56) Marsaglia, G.; Marsaglia, J. Evaluating the Anderson-Darling Distribution. *J. Stat. Softw.* **2004**, *9*, 1−5.

(57) Dallal, G. E.; Wilkinson, L. An Analytic Approximation to the Distribution of Lilliefors's Test Statistic for Normality. *Am. Stat.* **1986**, *40*, 294−296.

(58) Jarque, C. M.; Bera, A. K. Efficient Tests for Normality, Homoscedasticity and Serial Independence of Regression Residuals. *Econ. Lett.* **1980**, *6*, 255−259.

(59) SHAPIRO, S. S.; WILK, M. B. An Analysis of Variance Test for Normality (Complete Samples)†. *Biometrika* **1965**, *52*, 591−611.

(60) Brown, M. B.; Forsythe, A. B. Robust Tests for the Equality of Variances. *J. Am. Stat. Assoc.* **1974**, *69*, 364−367.

(61) Kruskal, W. H.; Wallis, W. A. Use of Ranks in One-Criterion Variance Analysis. *J. Am. Stat. Assoc.* **1952**, *47*, 583−621.

(62) Sachs, L. Einführung in die Statistik. In *Angewandte Statistik*; Springer: Berlin, Heidelberg, 1997; pp. 11−15. DOI: 10.1007/978-3-662-05746-9_2.

(63) Ruxton, G. D.; Beauchamp, G. Time for Some a Priori Thinking about Post Hoc Testing. *Behav. Ecol.* **2008**, *19*, 690−693.